Supplementary Information

Isotropically conducting tetraaryl osmium(IV), silane, and methane molecular wire junctions

Luana Zagami,[a] Cynthia Avedian,[a] Mukund Sharma,[a] Andrew Fraire,[a] Clarissa Olivar,[a] Daniel Hernangómez-Pérez,[b,*] and Michael S. Inkpen[a,*]

[a] *Department of Chemistry, University of Southern California, Los Angeles, CA 90089, USA*

[b] *CIC nanoGUNE BRTA, Tolosa Hiribidea, 76, 20018 Donostia-San Sebastián, Spain*

E-mail: d.hernangomez@nanogune.eu, inkpen@usc.edu

Contents

1. General Information

Synthetic Methods

Manipulations under a nitrogen atmosphere were carried out in oven-dried glassware using standard Schlenk line techniques. No special precautions were taken to exclude air or moisture during workup unless otherwise stated. Tetrahydrofuran (THF) was sparged with nitrogen and dried using a two-column solvent purification system packed with alumina (Pure Process Technologies, Nashua, NH, USA). N,N-Dimethylformamide (DMF) was purified by vacuum distillation, dried over 3Å molecular sieves,[1] and stored under nitrogen. Molecular sieves were activated by heating for ≥3.5 h at 350°C in a muffle furnace (Thermolyne, Thermo Scientific, Asheville, NC, USA), and stored in a desiccator until use. Grignard reagents were commercially available, or prepared according to the general method described in previous literature,[2] and titrated using a salicylaldehyde phenylhydrazone indicator to determine their concentration prior to use.[3] $(Oct_4N)_2[OsBr_6]$,[2] tetrakis(4-bromo-2,5-dimethylphenyl)osmium(IV),[4] tetrakis(4-bromophenyl)silane,[5] and (4'-(methylthio)-[1,1'-biphenyl]-4-yl)(triphenylphosphine)gold(I) (**Au2**)[6] were prepared using established literature procedures. Other reaction solvents (sparged with nitrogen prior to use) and chemical reagents were commercially available and used without further purification. 18.2 MΩ water was generated using an Arium® Mini Plus UV ultrapure water system (Sartorius AG, Goettingen, Germany). Deuterated solvents were purchased from Cambridge Isotope Laboratories, Inc., Cambridge Isotope Laboratories, Tewksbury, MA USA. Flash chromatography was performed using a Pure C-850 FlashPrep chromatography system and FlashPure EcoFlex flash cartridges (silica, irregular 50-75 μm particle size, 50-70 Å pore size; BUCHI Corporation, New Castle, DE, USA). Reaction yields are unoptimized.

^{1}H and ^{13}C{^{1}H} NMR spectra were recorded at room temperature on Varian VNMRS 500 (500 MHz), VNMRS 400 (400 MHz), or Mercury 400 (400 MHz) NMR spectrometers. ^{1}H NMR data recorded in $CDCl_3$ and CD_2Cl_2 is referenced to residual internal $CHCl_3$ (δ 7.26) and CH_2Cl_2 (δ 5.32) solvent signals.[7] ^{13}C{^{1}H} NMR data recorded in $CDCl_3$ and CD_2Cl_2 is referenced to internal $CDCl_3$ (δ 77.16) and CD_2Cl_2 (δ 53.52).[7] ^{1}H and ^{13}C{^{1}H} resonances were assigned where possible for new compounds using 2D correlation spectroscopy experiments. Mass spectrometry analyses were performed on a Waters GCT Premier (EI), JEOL Accu-TOF JMS-T2000GC (EI), Waters Synapt G2-Si (ESI), Bruker Autoflex Speed LRF (MALDI), or Bruker Daltonics

UltrafleXtreme (MALDI) at the Mass Spectrometry Lab, University of Illinois Urbana-Champaign.

Scanning Tunnelling Microscope-based Break Junction (STM-BJ)

These details are reproduced here from a previous report, with only minor changes, for convenience.[8] STM–BJ measurements were performed using custom-built setups that have been described previously,[9–11] operated in ambient atmosphere at room temperature. Hardware was controlled and analyses were performed using custom software (written using IgorPro, Wavemetrics Inc., OR, USA). Tip–substrate distances were controlled with sub-angstrom precision using a single-axis preloaded piezoelectric actuator (P-840.1, Physik Instrumente, MA, USA). Tunnelling currents were measured using a DLPCA-200 variable gain low noise transimpedance current amplifier (FEMTO Messtechnik GmbH, Berlin, Germany). Applying a bias between the tip and substrate, conductance was measured as a function of tip–substrate displacement (at 40 kHz acquisition rate) as the tip was repeatedly pushed into the substrate to reach a conductance of >5 G_0 (where $G_0 = 2e^2/h$) and then retracted 5–10 nm (at 20 nm/s) to break the contact. The resulting conductance-distance traces were compiled into 1D conductance histograms (using 100 bins/decade along the conductance axis), or 2D conductance-distance histograms (using 100 bins/decade along the conductance axis and 1000 bins/nm along the displacement axis). Traces in 2D histograms were aligned such that displacement = 0 nm where $G = 0.5\ G_0$. Color scales inset in 2D histograms are in count/1000 traces. Most probable conductance values for molecules studied here were obtained through Gaussian fits to their corresponding conductance peaks in 1D histograms. All histograms were constructed from ≥5,000 traces, unless otherwise stated.

STM tips were prepared from freshly cut Au wire (Ø = 0.25 mm; 99.998%, Alfa Aesar, MA, USA or 99.999%, Beantown Chemical, NH, USA). Substrates were prepared from evaporation of 100-200 nm Au (99.9985%, Alfa Aesar, or 99.999%, Angstrom Engineering Inc., ON, Canada) at a rate of ~1 Å/s onto mechanically polished AFM/STM steel specimen discs (Ted Pella Inc., CA, USA) with a COVAP Physical Vapor Deposition System (Angstrom Engineering Inc.) used exclusively for metal evaporation. Gold substrates were UV-ozone cleaned (Probe and Surface Decontamination Standard System, Novascan Technologies, Inc., IA, USA) and used for measurements that same day. Directly before starting a solution measurement, ≥1,000 traces were collected to check the electrode surfaces were free from contamination. Analytes were typically

studied as solutions (0.1-1 mM) in 1,2,4-trichlorobenzene (TCB; Millipore-Sigma, ≥99%), tetradecane (TD; Millipore-Sigma, >99%), or propylene carbonate (PC; Millipore-Sigma, anhydrous, ≥99.7%).

STM-BJ measurements in PC utilized a tip coated in Apiezon wax to minimize background capacitive and Faradaic currents. Voltammetry experiments using a coated gold STM tip as working electrode and gold substrate as counter and reference electrode were performed using a EmStat3+ potentiostat (PalmSens BV, Houten, The Netherlands).

Standard Electrochemical Methods

Standard electrochemical measurements were performed under an argon atmosphere using a CHI760E bipotentiostat (CH Instruments, Austin, TX, USA) with argon or nitrogen-sparged solutions of 0.1 M tetrabutylammonium hexafluorophosphate (^{n}Bu$_4$NPF$_6$) in CH_2Cl_2. Unless otherwise stated, plotted equilibrium voltammograms were obtained at a scan rate of 0.1 V s^{-1} and are not corrected for iR_s. Studies employed glassy carbon disc working electrodes (Ø = 3 mm, CH Instruments), mechanically polished using an alumina slurry prior to use. Pt wire reference and counter electrodes were cleaned by annealing in an oxyhydrogen flame. Analyte solutions were between 0.1-1 mM. Potentials are reported relative to $[Cp_2Fe]^+/[Cp_2Fe]$, measured against an internal Cp*$_2$Fe reference (−0.532 mV vs $[Cp_2Fe]^+/[Cp_2Fe]$).

Computational Details

Tunnel Coupling

Density functional theory (DFT) calculations were performed using the Q-Chem 5.4.2 program, using the molecular editor and visualization package IQMol 2.15.1.[12] Input structures of simplified **Os1**, **Si1**, and **C1** models comprising just two thioether contact groups – **Os1h**, **Si1h**, and **C1h**, respectively – were constructed by addition of those groups to the parent structures determined through single-crystal X-ray diffraction.[2,13,14] The geometries of these input structures were subsequently separately optimized without gold clusters at the PBE or B3LYP level of theory, using in each case a 6-31G** basis for light atoms and LACVP for osmium (and for gold, below). Isosurface plots for the frontier orbitals of these isolated molecules calculated using the B3LYP functional are provided in **Figure S11**.

Single gold atoms were next added, linked to the sulfur atoms of these structures, which were then subjected to further geometry optimization with both functionals. The difference in

energies between the HOMO and LUMO levels of the molecules bound to the Au_1 clusters (= 2t, a measure of the tunnel coupling[15,16]) was used to calculate $4t^2$. Isosurface plots for these frontier orbitals, calculated using the B3LYP functional, are provided for the **Os1h** model bound to Au_1 clusters in **Figure S12**.

Geometry optimizations were considered converged when the gradient, and either the energy or atomic displacement, satisfied the convergence criteria (energy = 10×10^{-8}, gradient = 10×10^{-6}, atomic displacement = 1200×10^{-6}; all values in atomic units [a.u.]). Unless otherwise stated, calculations used the direct inversion in the iterative subspace (DIIS) self-consistent field (SCF) optimization algorithm, using an on-the-fly (automated) superposition of atomic densities (AUTOSAD) initial guess. The SCF cycle was considered converged when the wave function error between consecutive SCF cycles was less than 10^{-8} a.u. When using the PBE functional, the geometries of model compounds bound to Au_1 clusters were optimized using the geometric direct minimization (GDM) self-consistent field optimization algorithm. The SCF cycle was considered converged when the wave function error between consecutive SCF cycles was less than 10^{-4} a.u.

Ab Initio Quantum Transport Calculations Details

Our ab initio transport calculations were performed using the FHI-aims package,[17] which implements a closed-shell formulation of Kohn-Sham density functional theory. We employed the PBE exchange-correlation functional[18] as a non-empirical, generalized gradient approximation to the exchange-correlation energy. Scalar relativistic effects were included through the zeroth-order regular approximation (ZORA) to account for relativistic corrections to the kinetic energy.[19] FHI-aims employs an optimized all-electron numeric atom-centered basis set. For this study, we considered the "light" computational settings, which correspond roughly to double-zeta basis set quality. The ground-state calculations were converged using reliable criteria for the self-consistent field cycle: 10^{-5} electrons/Å^3, for the difference in the particle density between consecutive SCF iterations; 10^{-7} eV, for the difference in the total energy; 10^{-4} eV, for the difference of the sum of Kohn-Sham eigenvalues and 10^{-4} eV/Å, for the difference of the forces.

The geometries of the model molecular junctions were determined using a well-established two-step process. First, the positions of the molecular atoms and the apex of the electrodes were optimized using the trust-radius enhanced variant of the Broyden-Fletcher-Goldfarb-Shanno algorithm[17] implemented in FHI-aims. For this optimization, we employ pyramidal gold clusters consisting of up to 11 gold atoms per pyramid. The molecular junction geometries were considered

to be structurally relaxed only when all the components of the residual forces per atom were below the threshold value of 10^{-2} eV/Å. Next, the optimized molecular and tip geometries from previous step were held fixed while additional layers of gold atoms were added to the outer planes of the previously optimized electrode tips. This ensures proper screening of excess charge and accurate level alignment for the subsequent quantum transport calculations.

The energy-dependent electronic transmission functions were computed within the linear response regime using the non-equilibrium Green's function formalism, as implemented in the AITRANSS transport module.[20–22] Each junction electrode was represented by a pyramidal face-centered cluster consisting of 37 atoms, cut from a crystal grown in the (111) direction with closest interatomic distance of 2.88 Å. The electrode self-energies were approximated by an energy-independent (Markovian) local model, given by $\Sigma(\mathbf{r}, \mathbf{r}') = i\eta(\mathbf{r})\delta(\mathbf{r} - \mathbf{r}')$. The local absorption rate, $\eta(\mathbf{r})$, was fine-tuned to ensure that the electronic transmission remained stable under smooth, moderate variations in $\eta(\mathbf{r})$ and was considered to be nonzero only in the subspace corresponding to the outermost layers of the finite cluster.

2. Synthetic Details

Tetrakis(2,5-dimethyl-4'-(methylthio)-[1,1'-biphenyl]-4-yl)osmium(IV) ***(Os2)***

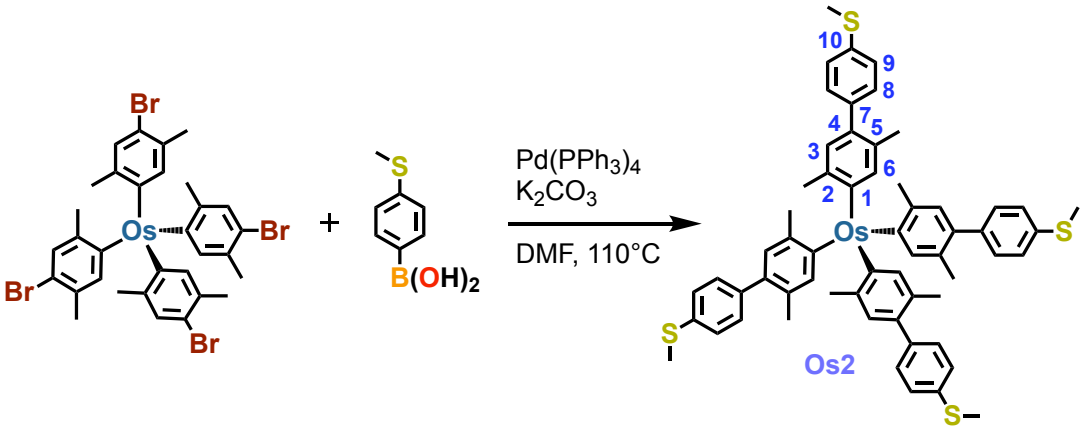

This compound was prepared using an adapted literature method.[23] A mixture of tetrakis(4-bromo-2,5-dimethylphenyl)osmium(IV) (0.166 g, 0.179 mmol), 4-(methylthio)phenylboronic acid (0.196 g, 1.17 mmol), $Pd(PPh_3)_4$ (0.083 g, 0.072 mmol), and K_2CO_3 (0.143 g, 1.03 mmol) in DMF (5 mL) was heated with stirring to 110°C for 3 d. After cooling to room temperature, solvent was removed under vacuum. The crude product was dissolved in CH_2Cl_2, pre-absorbed on Celite, then purified by column chromatography on a hexanes-packed SiO_2 column, eluting with 0:1→1:1 v/v CH_2Cl_2-hexanes. R_f = 0.30 (SiO_2, 1:1 v/v CH_2Cl_2-hexanes). Removal of solvent from selected fractions provided a black solid (0.067 g, 34%). ^{1}H NMR (CD_2Cl_2, 400 MHz): δ (ppm) δ 7.31 (s, 16H, aryl $C_{8/9}$-*H*), 6.83 (s, 4H, aryl C_6-*H*), 6.76 (s, 4H, aryl C_3-*H*), 2.52 (s, 12H, -SC*H*$_3$), 2.44 (s, 12H, C_2-C*H*$_3$), 2.26 (s, 12H, C_5-C*H*$_3$). ^{13}C{^{1}H} NMR (CD_2Cl_2, 100 MHz): δ (ppm) 141.39 (aryl, *C*$_4$-aryl), 138.28 (aryl), 138.12 (aryl), 138.06 (aryl), 137.60 (aryl, *C*$_{10}$-SMe), 135.92 (aryl, *C*$_6$-H), 131.28 (aryl, *C*$_5$-Me), 130.49 (aryl, *C*$_{8/9}$-H), 129.28 (aryl, *C*$_3$-H), 126.47 (aryl, *C*$_{8/9}$-H), 25.62 (C_2-*C*H$_3$), 20.55 (C_5-*C*H$_3$), 15.99 (-S*C*H$_3$). HR-MS (MALDI+) *m/z*: 1100.3193 ([M]$^+$ calc. for $C_{60}H_{60}OsS_4$: 1100.3193).

Tetrakis(2,5-dimethyl-4''-(methylthio)-[1,1':4',1''-terphenyl]-4-yl)osmium(IV) (***Os3***)

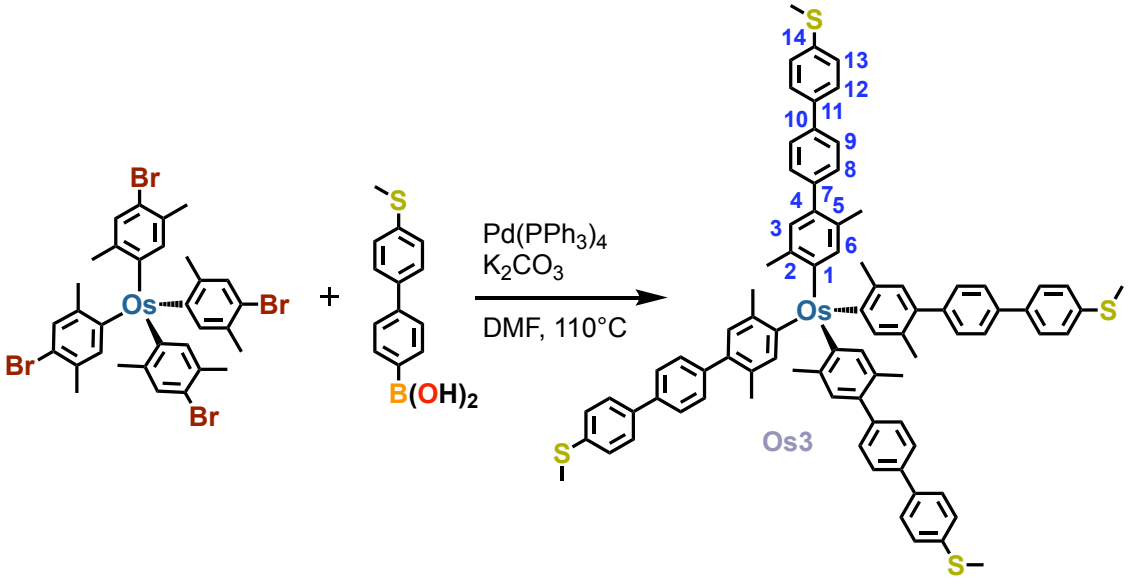

This compound was prepared using an adapted literature method.[23] A mixture of tetrakis(4-bromo-2,5-dimethylphenyl)osmium(IV) (0.097 g, 0.105 mmol), 4-(4-methylthiophenyl)phenylboronic acid (0.165 g, 0.676 mmol), $Pd(PPh_3)_4$ (0.063 g, 0.055 mmol), and K_2CO_3 (0.095 g, 0.687 mmol) in DMF (5 mL) was heated with stirring to 110°C for 3 d. After cooling to room temperature, solvent was removed under vacuum. The crude product was dissolved in CH_2Cl_2, pre-absorbed on Celite, then purified by column chromatography on a hexanes-packed SiO_2 column, eluting with 0:1→1:1 v/v CH_2Cl_2-hexanes. R_f = 0.22 (SiO_2, 1:1 v/v CH_2Cl_2-hexanes). Removal of solvent from selected fractions provided a black solid (0.017 g, 12%) that was subsequently stored at −20°C. ^{1}H NMR ($CDCl_3$, 400 MHz): δ (ppm) 7.63 (d, 8H, *J* = 8.4 Hz, aryl-*H*), 7.59 (d, 8H, *J* = 8.4 Hz, aryl-*H*), 7.46 (d, 8H, *J* = 8.4 Hz, aryl-*H*), 7.35 (d, 8H, *J* = 8.5 Hz, aryl-*H*), 6.94 (s, 4H, aryl C_6-*H*), 6.80 (s, 4H, aryl C_3-*H*), 2.54 (s, 12H, -SC*H*$_3$), 2.47 (s, 12H, C_2-C*H*$_3$), 2.31 (s, 12H, C_5-C*H*$_3$). ^{13}C{^{1}H} NMR ($CDCl_3$, 101 MHz): δ (ppm) 141.08 (aryl, *C*$_4$-aryl), 140.39 (aryl, *C*$_7$-aryl), 138.95 (aryl), 138.23 (aryl), 138.03 (aryl), 137.79 (aryl), 137.71 (aryl), 136.57 (aryl, *C*$_6$-H), 130.84 (aryl, *C*$_5$-Me), 130.35 (aryl *C*$_{8/9}$-H), 129.09 (aryl, *C*$_3$-H), 127.53 (aryl *C*-H), 127.12 (aryl *C*-H), 126.50 (aryl *C*-H), 25.69 (C_2-*C*H$_3$), 20.61 (C_5-*C*H$_3$), 16.07 (-S*C*H$_3$). HR-MS (MALDI+) *m/z*: 1404.4428 ([M]$^+$ calc. for $C_{84}H_{76}OsS_4$: 1404.4445).

Tetrakis(4-(methylthio)phenyl)silane ***(Si1)***

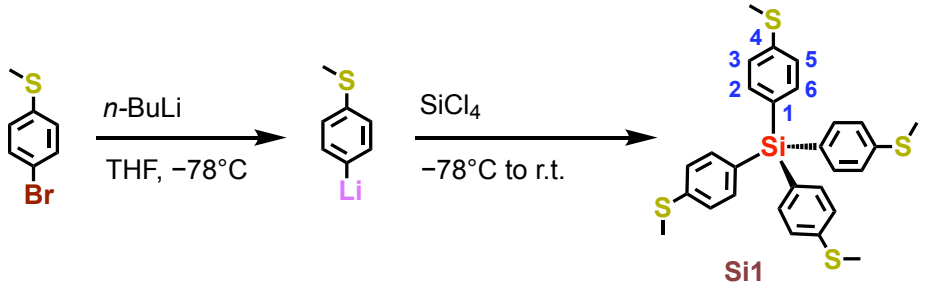

This compound was prepared using adapted literature methods.[5] 2.5 M *n*-BuLi in hexanes (4.70 mL, 11.8 mmol) was added dropwise at −78°C to a stirred solution of 4-bromothioanisole (2.612 g, 12.86 mmol) in THF (10 mL). After 1 h at −78°C, silicon tetrachloride (0.30 mL, 2.6 mmol) was added to the reaction mixture, which was stirred at −78°C for an additional 1 h then at room temperature for 1 d. Solvent was removed by rotary evaporation, whereby the crude product was dissolved in CH_2Cl_2, pre-absorbed on Celite, then purified by column chromatography on a hexanes-packed SiO_2 column, eluting with 0:1→1:1 v/v CH_2Cl_2-hexanes. R_f = 0.18 (SiO_2, 1:1 v/v CH_2Cl_2-hexanes). Removal of solvent from selected fractions provided a white solid (0.028 g, 2%). ^{1}H NMR (CD_2Cl_2, 500 MHz): δ (ppm) 7.48 (d, 8H, *J* = 8.3 Hz, aryl $C_{2/6}$-*H*), 7.18 (d, 8H, *J* = 7.5 Hz, aryl $C_{3/5}$-*H*), 2.47 (-SC*H*$_3$). ^{13}C{^{1}H} NMR (CD_2Cl_2, 101 MHz): δ (ppm) 142.60 (aryl, *C*$_4$-SMe), 134.87 (aryl, *C*-H), 129.86 (aryl, *C*$_1$-Si), 125.40 (aryl, *C*-H), 15.05 (-S*C*H$_3$). HR-MS (EI+) *m/z*: 520.0851 (weak, $[M]^+$ calc. for $C_{28}H_{28}S_4Si$: 520.0843).

Tetrakis(4'-(methylthio)-[1,1'-biphenyl]-4-yl)silane ***(Si2)***

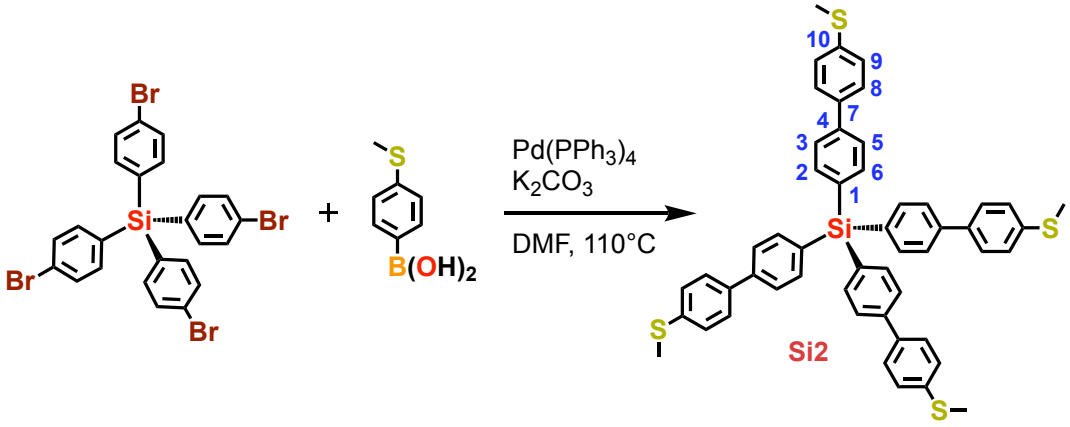

This compound was prepared using an adapted literature method.[23] A mixture of tetrakis(4-bromophenyl)silane (0.109 g, 0.167 mmol), 4-(methylthio)phenylboronic acid (0.158 g, 0.940 mmol), $Pd(PPh_3)_4$ (0.074 g, 0.064 mmol), and K_2CO_3 (0.137 g, 0.991 mmol) in DMF (5 mL) was

heated with stirring to 110°C for 3 d. After cooling to room temperature, solvent was removed under vacuum. The crude product was dissolved in CH_2Cl_2, pre-absorbed on Celite, then purified by column chromatography on a hexanes-packed SiO_2 column, eluting with 0:1→1:1 v/v CH_2Cl_2-hexanes. R_f = 0.27 (SiO_2, 1:1 v/v CH_2Cl_2-hexanes). Removal of solvent from selected fractions provided a white solid (0.041 g, 30%). ^{1}H NMR (CD_2Cl_2, 400 MHz): δ (ppm) 7.72 (d, 8H, *J* = 8.3 Hz, aryl-*H*), 7.66 (d, 8H, *J* = 8.5 Hz, aryl-*H*), 7.59 (d, 8H, *J* = 8.7 Hz, aryl-*H*), 7.34 (d, 8H, *J* = 8.7 Hz, aryl-*H*), 2.52 (-SC*H*$_3$). ^{13}C{^{1}H} NMR (CD_2Cl_2, 101 MHz): δ (ppm) 142.05 (aryl, *C*-R), 138.78 (aryl, *C*$_{10}$-SMe), 137.64 (aryl, *C*-R), 137.28 (aryl, *C*-H), 133.18 (aryl, *C*-R), 127.79 (aryl, *C*-H), 127.03 (aryl, *C*-H), 126.64 (aryl, *C*-H), 15.84 (-S*C*H$_3$). HR-MS (MALDI+) *m/z*: 824.2084 ([M]$^+$ calc. for $C_{52}H_{44}S_4Si$: 824.2095).

Tetrakis(4-(methylthio)phenyl)methane ***(C1)***

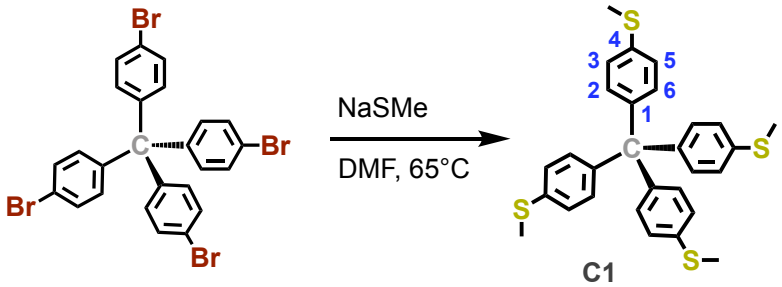

This compound was prepared using an adapted literature method.[24] A solution of tetrakis(4-bromophenyl)methane (0.201 g, 0.316 mmol) in DMF (2 mL) was added to solution of sodium thiomethoxide (0.135 g, 1.93 mmol) in DMF (2 mL). The resulting mixture was heated to 65°C and stirred for 1 d. After cooling, solvent was removed under vacuum. The crude product was dissolved in CH_2Cl_2, pre-absorbed on Celite, then purified by column chromatography on a hexanes-packed SiO_2 column, eluting with 0:1→1:1 v/v CH_2Cl_2-hexanes. R_f = 0.30 (SiO_2, 1:1 v/v CH_2Cl_2-hexanes). Removal of solvent from selected fractions provided a white solid (0.027 g, 17%). ^{1}H NMR (CD_2Cl_2, 400 MHz): δ (ppm) 7.12 (s, 16H, aryl-*H*), 2.45 (s, 12H, -SC*H*$_3$). ^{13}C{^{1}H} NMR (CD_2Cl_2, 101 MHz): δ (ppm) 143.72 (aryl, *C*$_1$-C(*sp*^{3})), 136.68 (aryl, *C*$_4$-SMe), 131.59 (aryl, *C*-H), 125.73 (aryl, *C*-H), 15.66 (-S*C*H$_3$). HR-MS (ESI+) *m/z*: 504.1066 ([M]$^+$ calc. for $C_{29}H_{28}S_4$: 504.1074).

Tetrakis(4'-(methylthio)-[1,1'-biphenyl]-4-yl)methane ***(C2)***

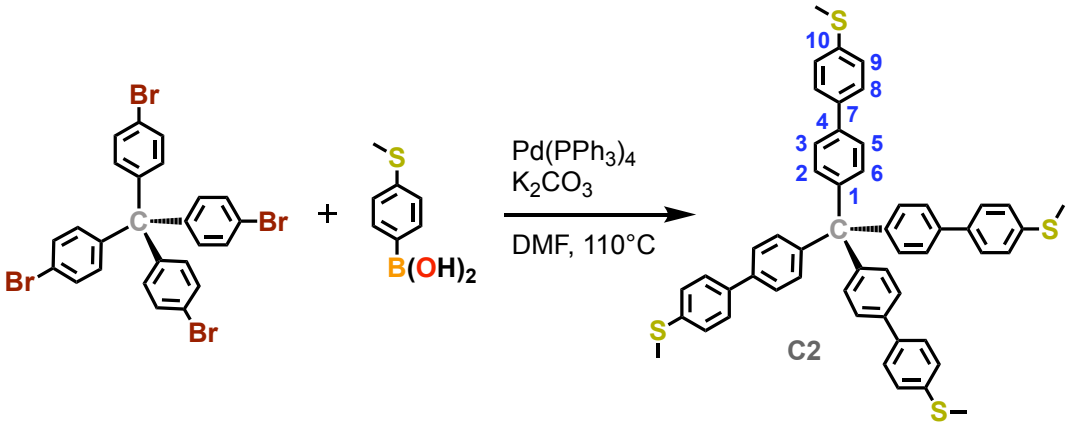

This compound was prepared using an adapted literature method.[23] A mixture of tetrakis(4-bromophenyl)methane (0.111 g, 0.175 mmol), 4-(methylthio)phenylboronic acid (0.180 g, 1.07 mmol), $Pd(PPh_3)_4$ (0.073 g, 0.063 mmol), and K_2CO_3 (0.131 g, 0.948 mmol) in DMF (5 mL) was heated with stirring to 110°C for 3 d. After cooling to room temperature, solvent was removed under vacuum. The crude product was dissolved in CH_2Cl_2, pre-absorbed on Celite, then purified by column chromatography on a hexanes-packed SiO_2 column, eluting with 0:1→1:1 v/v CH_2Cl_2-hexanes. R_f = 0.25 (SiO_2, 1:1 v/v CH_2Cl_2-hexanes). Removal of solvent from selected fractions provided a white solid (0.013 g, 9%). ^{1}H NMR ($CDCl_3$, 500 MHz): δ (ppm) 7.53 (m, 16H, aryl-*H*), 7.38 (d, 4H, *J* = 8.5 Hz, aryl-*H*), 7.31 (d, 4H, *J* = 8.5 Hz, aryl-*H*), 2.52 (s, 12H, -SC*H*$_3$). ^{13}C{^{1}H} NMR ($CDCl_3$, 126 MHz): δ (ppm) 145.84 (aryl, *C*R$_3$), 138.14 (aryl, *C*R$_3$), 137.71 (aryl, *C*R$_3$), 137.48 (aryl, *C*R$_3$), 131.67 (aryl, *C*-H), 127.43 (aryl, *C*-H), 127.06 (aryl, *C*-H), 126.06 (aryl, *C*-H), 16.02 (-SCH$_3$). HR-MS (EI+) *m/z*: 808.2321 ([M]$^+$ calc. for $C_{53}H_{44}S_4$: 808.2326).

3. Electrochemistry

Table S1. Electrochemical data for selected Os(aryl)$_4$ complexes.[a]

	redox transition	$E_{1/2}$ (V)	E_{pa} (V)	E_{pc} (V)	ΔE (V)	i_{pa}/i_{pc}	ref.
Os(C_8H_8-SMe)$_4$ (**Os1**)	1−/0	−1.955	−1.920	−1.990	0.070	0.94	[25]
	0/1+	+0.018	+0.056	−0.020	0.076	0.99	
	1+/2+	+0.650	+0.700	+0.600	0.100	0.98	
Os(C_8H_8-C_6H_4-SMe)$_4$ (**Os2**)	1−/0	−1.906	−1.868	−1.944	0.076	1.05	this work
	0/1+	+0.228	+0.271	+0.186	0.085	1.02	
	1+/2+	-	-	-	-	-	
Os(C_8H_8-C_6H_4-C_6H_4-SMe)$_4$ (**Os3**)	1−/0	−1.927	−1.861	−1.994	0.133	1.02	this work
	0/1+	+0.222	+0.273	+0.172	0.101	1.02	
	1+/2+	-	-	-	-	-	
Os(C_8H_9)$_4$	1−/0	−2.008	−1.969	−2.047	0.078	0.98	[2]
	0/1+	+0.244	+0.281	+0.208	0.073	1.00	
	1+/2+	-	-	-	-	-	
Os(C_8H_8-C_6H_4-C_6H_5)$_4$	1−/0	-	-	-	-	-	[26]
	0/1+	+0.21	-	-	-	-	
	1+/2+	+1.05	-	-	-	-	

[a] Scan rate = 0.1 V s^{-1}; Supporting electrolyte = ^{n}Bu$_4$NPF$_6$-CH_2Cl_2; working electrode: glassy carbon; reference electrode, counter electrode: Pt. All potentials are reported relative to $[Cp_2Fe]^+/Cp_2Fe$, corrected for iR_s.

4. UV-Vis Spectroscopy

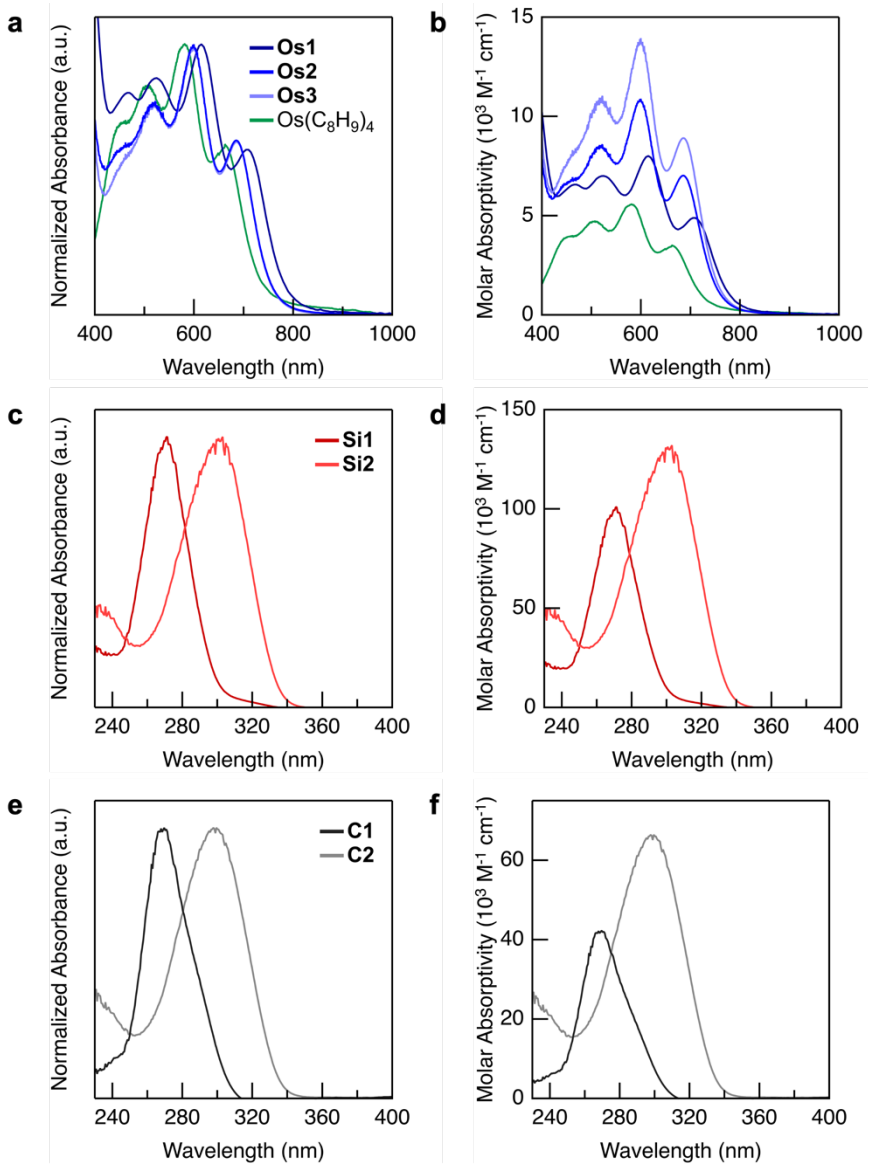

Figure S1. (a-b) Overlaid UV-vis spectra for **Os1**, **Os2**, **Os3**, and Os(xylyl)$_4$[25] measured in CH_2Cl_2. In (a), absorbance spectra are normalized to the peak of maximum intensity in the visible region. Data for **Os1-3** are reproduced from **Figure 2c** for convenience. In (b), plots of molar absorptivity against wavelength reveal the extended complexes are more efficient at absorbing visible light. **(c-d)** Analogous plots for **Si1** and **Si2**. **(e-f)** Analogous plots for **C1** and **C2**. Data extracted from these measurements are provided in **Table S2**.

Table S2. Spectroscopic and frontier orbital energy gap data for selected compounds.[a]

	λ_{max} (nm)	ε_{max} (M^{-1} cm^{-1})	E_{opt} (nm)[b]	E_{elec} (V) [c]	ref.
$Os(C_8H_8\text{-}SMe)_4$ (**Os1**)	465	6,568	784	1.973	[25]
	525	7,004			
	613	7,951			
	705	4,888			
$Os(C_8H_8\text{-}C_6H_4\text{-}SMe)_4$ (**Os2**)	462	6,707	758	2.134	this work
	516	8,560			
	598	10,872			
	685	7,020			
$Os(C_8H_8\text{-}C_6H_4\text{-}C_6H_4\text{-}SMe)_4$ (**Os3**)	452sh	7,838	757	2.149	this work
	519	10,890			
	598	13,889			
	685	8,902			
$Os(C_8H_9)_4$	454	3,857	744	2.252	[2], this work
	503	4,710			
	580	5,570			
	662	3,513			
$Si(C_6H_4\text{-}SMe)_4$ (**Si1**)	271	100,970 [d]	300	-	this work
$Si(C_6H_4\text{-}C_6H_4\text{-}SMe)_4$ (**Si2**)	303	132,090 [d]	335	-	this work
$C(C_6H_4\text{-}SMe)_4$ (**C1**)	270	42,277 [d]	304	-	this work
$C(C_6H_4\text{-}C_6H_4\text{-}SMe)_4$ (**C2**)	299	66,442 [d]	333	-	this work

[a] Measured in CH_2Cl_2. [b] Defined here as the longest wavelength at which absorbance reaches ~10% of the peak of maximum intensity in the visible region. [c] Calculated from solution electrochemical studies: $E_{elec} = E_{1/2}(0/1+) - E_{1/2}(1-/0)$. [d] High ε_{max} have been reported for other tetra(oligoaryl)silane and methane complexes. For example, 51,000 M^{-1} cm^{-1} for tetrakis(4-(thiophen-2-yl)phenyl)methane,[27] and up to 1.9×10^6 M^{-1} cm^{-1} for a tetra(pentaaryl)silane with ligand arms comprising fluorene groups.[28]

5. Additional Conductance Data

Table S3. Conductance values for selected compounds.[a]

	conductance (G_0)			
	TD		TCB	
compound/*geometry*	*intact molecule*	*dissociated ligand*	*intact molecule*	*dissociated ligand*
Os1 [b]	3.7×10^{-5}	6.5×10^{-3}	-	-
Si1 [b]	3.5×10^{-5}	6.6×10^{-3}	-	-
C1 [b]	2.0×10^{-5}	- [c]	-	-
Os2	1.9×10^{-6}	8.4×10^{-4}	- [d]	1.2×10^{-4}
Si2	3.5×10^{-7}	9.5×10^{-4}	4.3×10^{-7}	9.7×10^{-4}
C2	- [c]	7.6×10^{-4}	6.0×10^{-7}	8.6×10^{-4}
Os3	- [c]	1.2×10^{-4}	- [d]	1.5×10^{-4}

[a] All values from measurements at V_{bias} = 750 mV from peak fits to histograms (1), unless otherwise stated. [b] V_{bias} = 250 mV. [c] Peak not observed in conductance histograms. [d] Value not reported due to the large apparent conductance variability for this junction geometry when measured in this solvent.

Reproducibility Studies in TD

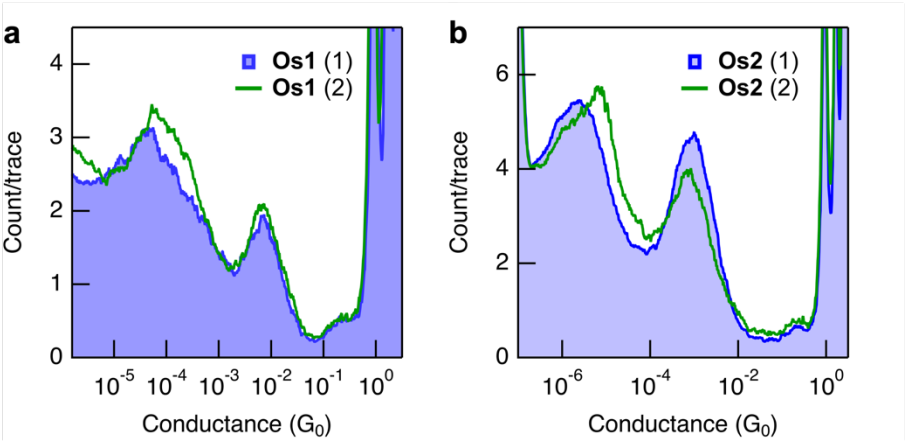

Figure S2. Overlaid 1D histograms for repeated conductance measurements of **(a) Os1** (V_{bias} = 250 mV) and **(b) Os2** (V_{bias} = 750 mV) in TD. This data suggests there is a greater consistency between measurements obtained using TD than TCB for these Os(aryl)$_4$ complexes (see **Figure S5**).

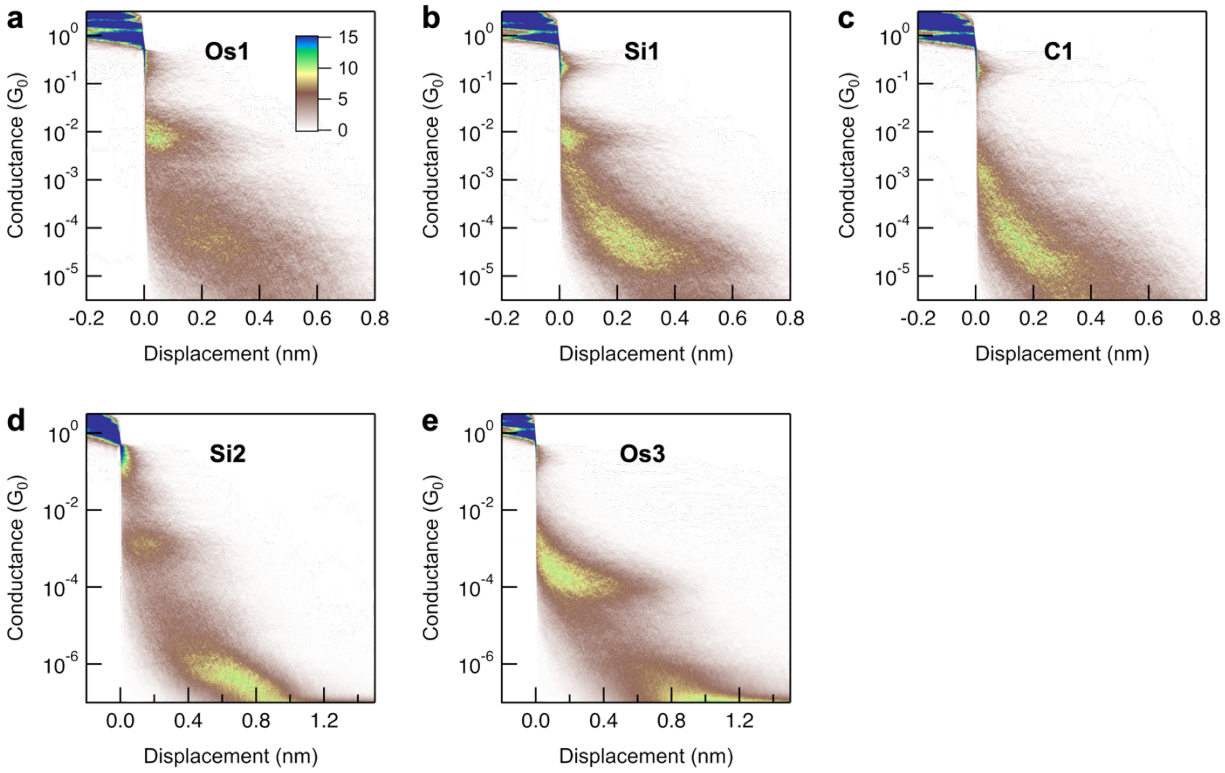

Figure S3. 2D histograms for **(a) Os1**, **(b) Si1**, **(c) C1** (V_{bias} = 250 mV), **(d) Si2**, and **(e) Os3** (V_{bias} = 750 mV), corresponding to the 1D histograms shown in **Figure 3**.

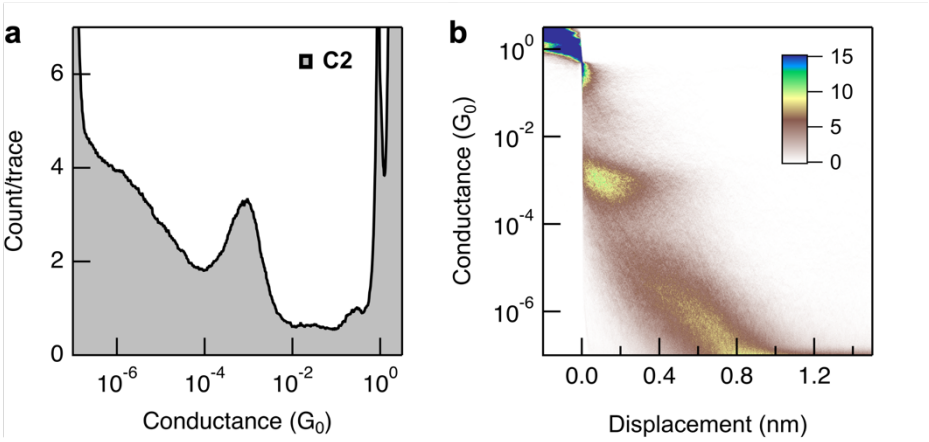

Figure S4. (a) 1D and **(b)** 2D histogram obtained for measurements of a solution of **C2** in TD (V_{bias} = 750 mV). Only the high conductance peak attributed to junctions comprising the dissociated biaryl is observed (**Figure S9**).

Reproducibility Studies in TCB

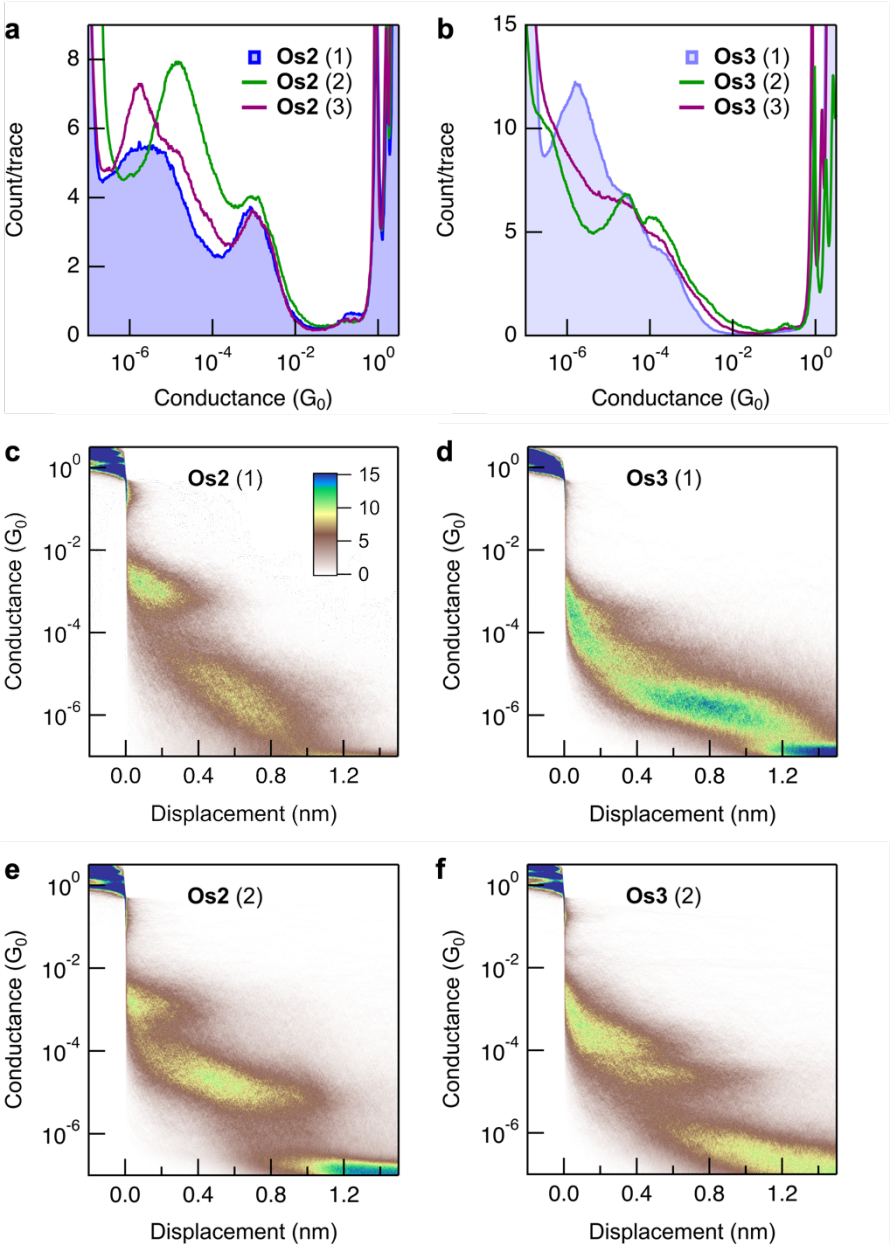

Figure S5. Overlaid 1D histograms for repeated conductance measurements of **(a) Os2** and **(b) Os3** in TCB at V_{bias} = 750 mV. **(c-f)** Example 2D histograms corresponding to selected 1D histograms in (a,b). This data shows that the low conductance features attributed to junctions comprising the intact complexes exhibit a large experiment to experiment variability when measured in TCB. The low conductance step observed for **Os3** extends to ~1.4 nm displacement. While this is shorter than the S-S distance of 2.6 nm calculated for this compound, it is close to the junction displacement expected if the difference in step length between **Os1** and **Os2** (~0.6 nm) is added to the displacement of **Os2** (~1 nm).

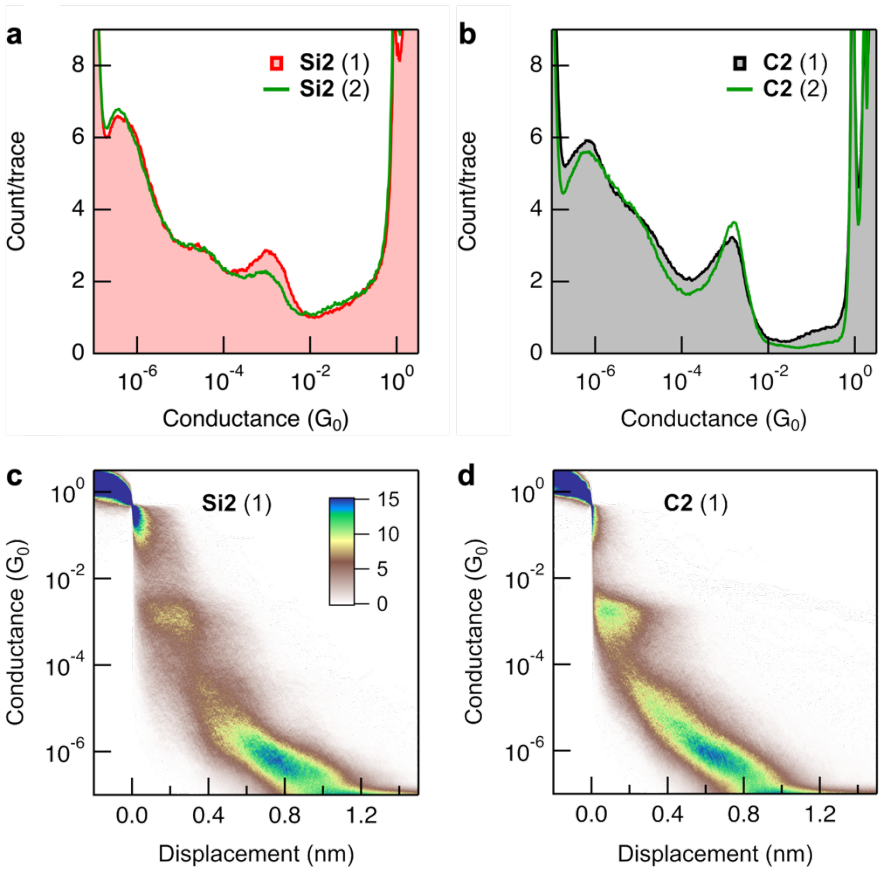

Figure S6. Overlaid 1D histograms for repeated conductance measurements of **(a) Si2** and **(b) C2** in TCB at V_{bias} = 750 mV. **(c-d)** Example 2D histograms corresponding to selected 1D histograms in panels (a) and (b). This data shows that the low conductance features attributed to junctions comprising the intact compounds exhibit a better reproducibility when measured in TCB than the Os(aryl)$_4$ complexes.

Analysis of High Conductance Features

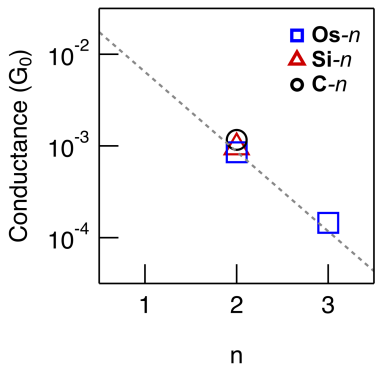

Figure S7. A plot of conductance versus number of aryl groups in each ligand for the high conductance peak feature observed in each series of wires **Os-*n***, **Si-*n***, **C-*n***, measured in TCB. Grey dashed line is the fit of conductance versus *n* for **Os-*n*** measured in TD (**Figure 3e**), included here for comparison.

To further evaluate the assignment of the high conductance peak features to cleaved linker arms, in **Figure S9** we overlay histograms obtained for conductance measurements of **Os2**, **Si2**, and **C2** with that of (4'-(methylthio)-[1,1'-biphenyl]-4-yl)(triphenylphosphine)gold(I) (**Au2**). This complex comprises the same biphenyl ligand as found in the tetrahedral compounds but now coordinated directly to a gold(I) center. This, as well as a series of analogous compounds, has previously been used to substantiate the formation of chemisorbed Au-C(sp^2) contacts from precursors comprising -$SnMe_3$,[29] -$B(OH)_2$,[30] or -I groups.[6] We find that the conductance of junctions formed from **Au2** are close to (albeit a factor of 2-3 higher than) those of the high conductance peaks formed through the proposed ligand dissociation reaction, further substantiating our assertion. We speculate that the slightly higher conductance value observed for **Au2** may be attributable to differences in solution/surface concentration, the methyl-substituents of dissociated **Os-*n*** ligands which may impose steric constraints on junction geometry, or the presence of coordinating phosphine. Differences in the chemical environment near the junction may influence the energetic alignment between the dominant conducting orbital and E_F, as observed for conductance measurements in different solvents,[8,31] resulting in small changes in the measured junction conductance.

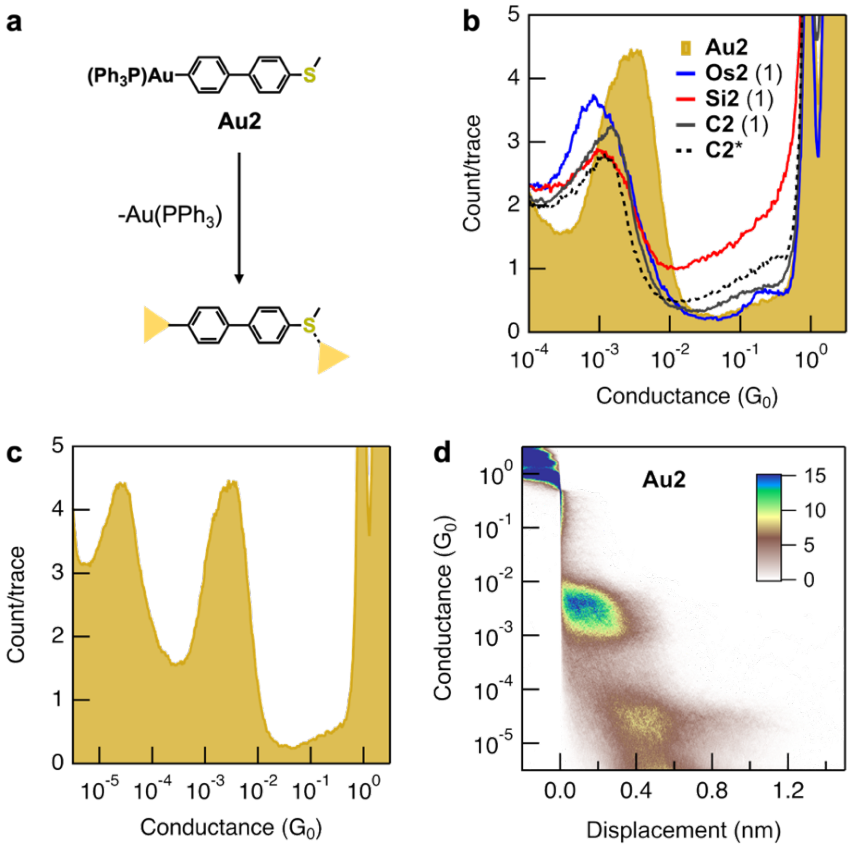

Figure S8. (a) Schematic showing junction formation from **Au2**, a complex containing a preinstalled Au-C bond. **(b)** Overlaid 1D histograms obtained measurements of **Os2**, **Si2**, and **C2** (solid lines, obtained with V_{bias} = 750 mV), now focused on the high conductance peak around 10^{-3} G_0, and **Au2** (filled, V_{bias} = 100 mV) in TCB (6,000-10,000 traces). An overlaid histogram of **C2** obtained at V_{bias} = 100 mV (**C2***, dashed, 10,000 traces) indicates the conductance of this peak does not exhibit a large bias dependence. The features for **Os2**, **Si2**, and **C2** are systematically lower in conductance (8.3 to 12.2 × 10^{-4} G_0) by a factor of 2-3 compared to the peak seen for **Au2** (25.3 × 10^{-4} G_0). **(c)** 1D and **(d)** 2D conductance histograms for **Au2**, plotted to a lower conductance range. The feature at 2.4 × 10^{-5} G_0 is attributed to junctions comprising the tetraphenylene dimer formed from the C(sp^2)-C(sp^2) homocoupling of two surface adsorbed MeS-C_6H_4-C_6H_4-Au species.

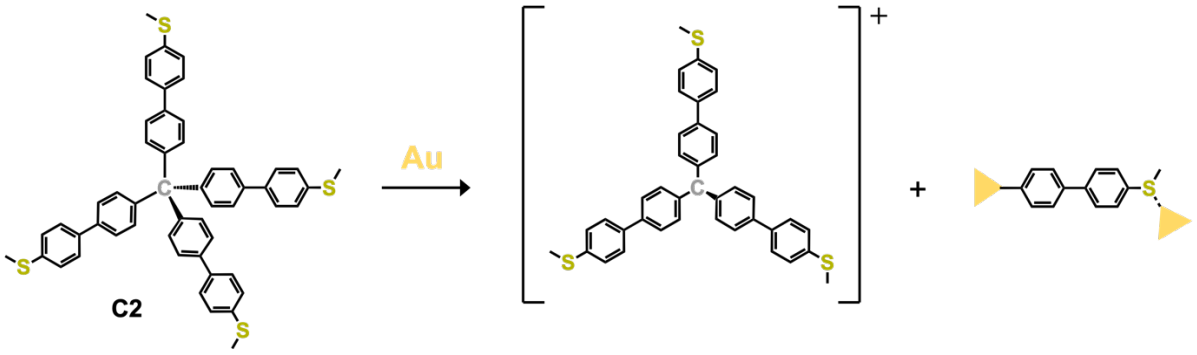

Figure S9. Proposed reaction leading to observed ligand dissociation, using **C2** as a representative example. The exact mechanism of C(sp^2)-central atom bond cleavage is unknown. However, we note that formation of an Au-C(sp^2) bond through direct interaction between a gold surface atom and the C(sp^2) atom of the intact complex(es) appears unfeasible due to steric hinderance.

Additional Measurements in Propylene Carbonate

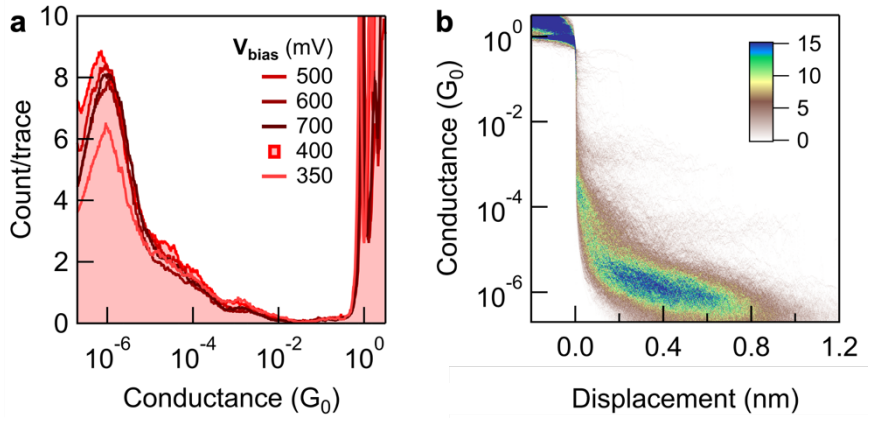

Figure S10. (a) Overlaid 1D histograms for **Si2** measured in propylene carbonate at different V_{bias} (2,000 traces; biases listed in chronological order). Much smaller conductance changes are observed compared to analogous measurements for **Os2**. No significant feature at ~1×10^{-3} G_0, attributed to junctions comprising dissociated oligoaryl ligand (see **Figure S9** and associated discussion), is observed. **(b)** A representative 2D histogram corresponding to the 1D histogram in panel (a) obtained at V_{bias} = 700 mV.

6. Additional Computational Data

Geometric Analysis

We note that the aryl groups of oligoaryl wires with tetrahedral osmium(IV), silane, or methane centers exhibit different geometric relationships to one another in the frozen geometries observed in molecular structures obtained from single-crystal X-ray crystallography or computational experiments. The relationship between two aryl substituents can be defined using two dihedral angles (α and β), as shown in **Figure S11**. There are six pairs of dihedral angles for each tetraaryl compound.

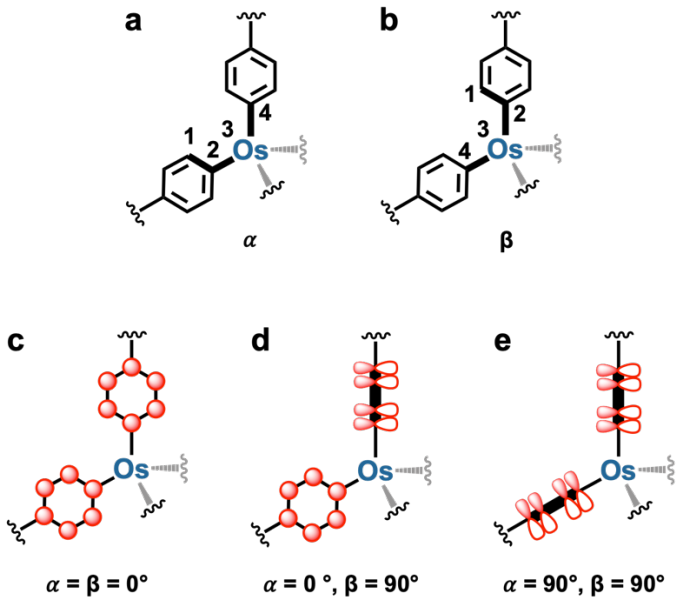

Figure S11. (a,b) The relative orientation of adjacent aryl ligands can be defined using two different dihedral angles, α and β. These angles are defined by atoms 1-4, connected in each schematic through bonds with bold linewidths. In each case, atom 1 was chosen as the aryl carbon atom closest to the bond defined by atoms 3 and 4. **(c-e)** Illustrations of different aryl-aryl orientations, highlighting how they may influence overlap/coupling between each aryl π-system, at selected values of α and β.

In **Table S4** we define these angle pairs for a self-consistent series of structurally characterized tetra(ferrocenylphenyl) compounds comprising Os(IV) (**Os-Fc**), C (**C-Fc**), or Si (**Si-Fc**) centers.[4] In **Table S5** we repeat the same analysis, now using parent compounds with the ferrocenyl substituents removed, after their geometry is optimized using computational methods (Q-Chem). Each series of compounds exhibits pairs of dihedral angles that are *similar* or *different* (denoted with black or blue text in the tables, respectively). We sought to establish whether these different classes of angle pairs might result in differences in electronic coupling between the aryl π-systems, plausibly modulating the calculated through-molecule transmission in their electrode-connected wires. We stress that the aryl rings are expected, based on NMR spectroscopic characterization, to be freely rotating in solution at room temperature.[4]

Table S4. Dihedral angles defining relative aryl ligand orientation in model tetraaryl compounds.[a]

	Angle Pair											
	1		2		3		4		5		6	
Os-Fc	−19.57	76.22	−42.26	−42.26	19.57	−76.22	42.26	42.26	76.22	−19.57	19.57	−76.22
Si-Fc	−64.54	28.21	54.58	54.58	−0.34	85.00	−36.86	−36.86	−0.34	85.00	28.21	−64.54
C-Fc	−0.57	−71.47	66.61	−5.19	−53.94	−48.28	50.45	51.60	72.91	−5.16	−69.71	6.51

[a] All values in degrees, obtained from a self-consistent set of X-ray crystal structures of ferrocene-appended tetraaryl complexes.[4] Blue angles = distinct dihedral angles in the pair, black = comparable dihedral angles.

Table S5. Dihedral angles defining relative aryl ligand orientation in tetraaryl compounds after geometry optimization (Q-Chem).[a]

	Angle Pair											
	1		2		3		4		5		6	
$Os(C_8H_9)_4$	−57.16	−58.43	62.73	2.33	−61.72	−0.74	58.02	57.18	65.22	1.36	−1.32	−64.63
$Si(C_6H_5)_4$	7.84	−37.84	82.28	−24.51	−82.28	24.51	37.84	37.84	82.28	−24.51	24.51	−82.28
$C(C_6H_5)_4$	64.75	1.52	−64.75	−1.52	−56.67	−56.67	−1.52	−64.75	56.67	56.67	64.75	1.52

[a] All values in degrees, obtained following geometry optimization of parent compounds (unfunctionalized aryl ligands), based on X-ray crystal structures obtained by different groups,[2,13,14] using PBE. Here both $Si(C_6H_5)_4$ and $C(C_6H_5)_4$ were optimized with S_4 symmetry. Ligands: C_6H_5 = phenyl; C_8H_9 = 2,5-xylyl. Blue angles = distinct dihedral angles in the pair, black = comparable dihedral angles.

Tunnel Coupling (Q-Chem)

We explored the properties of two sets of each model complex, **Os1h**, **Si1h**, **C1h**. One set exhibited a pair of aryl substituents that had *similar* pairs of dihedral angles, and the other set had angles pairs that were *different* (see *Geometric Analysis*, above). The process of constructing each model essentially involved adding two -SMe groups on different aryl substituents of the parent complex. In **Table S6** and **Table S7**, we present selected computational data for these model compounds obtained using the PBE and B3LYP functionals, respectively, both before and after adding Au_1 clusters.

We find that the HOMO-LUMO gap of each molecular complex does not strongly depend on whether the dihedral angle pair chosen is *similar* or *different*. This is easily rationalized given that this gap is a property of the entire molecule, and that the addition of -SMe substituents to different aryl rings of each molecule simply generates geometric isomers with very similar electronic structures. Here we observe the same trends in HOMO-LUMO gap as found using FHI-aims (**Table S8**). The gaps are always smaller for **Os1h** than for **Si1h**/**C1h**, and the gaps are larger for all models when using the B3LYP functional compared to PBE. Example isosurface plots for the frontier orbitals of each model are presented in **Figure S12**.

We use these models, now connected to Au_1 clusters through the sulfur atom of their -SMe substituents, to explore changes in their calculated tunnel couplings, 2t. The square of this quantity has been found to be proportional to the molecular junction conductance.[16,32] In agreement with our experimental conductance measurements for **Os2** and **Si2** in PC, and with the results of quantum transport calculations (below), we find the tunnel coupling for **Os1h**-Au_1 is consistently larger than for **Si1h**-Au_1 or **C1h**-Au_1 (**Table S6,7**). Notably, this difference is maximized when using the PBE functional, and tunnel couplings calculated using PBE are also more variable between models with *similar* or *different* dihedral angle pairs, relative to those with B3LYP. Representative isosurface plots for the tunnel coupled orbitals of **Os1h**-Au_1 are provided in **Figure S13**. While differences in tunnel coupling are observed for non-equivalent geometries in these simple models, transmission calculations for the same molecular structures connected between larger gold electrodes reveal these junctions exhibit the same calculated conductance (**Figure 16**).

Table S6. Selected computational data for **Os1h**, **Si1h**, **C1h** models using the PBE functional.[a]

	s/d [b]	α (°) [c]	β (°) [c]	HOMO (eV)	LUMO (eV)	gap (eV) [d]	$4t^2$ (eV^2)
Os1h	s	54.9	57.1	−3.817	−2.222	1.595	-
	d	−64.2	−0.3	−3.813	−2.242	1.571	-
Si1h	s	−38.5	−38.5	−4.867	−1.271	3.596	-
	d	−83.7	25.8	−4.857	−1.276	3.581	-
C1h	s	59.3	59.3	−4.642	−1.144	3.498	-
	d	−72.9	9.4	−4.770	−1.284	3.487	-
Os1h-Au_1	s	49.5	50.6	−3.854	−3.741	-	1.3×10^{-2}
	d	−60.8	−4.0	−3.845	−3.728	-	1.4×10^{-2}
Si1h-Au_1	s	−47.1	−39.5	−3.971	−3.964	-	4.5×10^{-5}
	d	−80.1	39.4	−3.972	−3.949	-	5.3×10^{-4}
C1h-Au_1	s	64.8	64.0	−3.976	−3.903	-	5.4×10^{-3}
	d	−75.9	12.6	−3.943	−3.933	-	9.3×10^{-5}

[a] Calculations performed as described in *Computational Details*. [b] Here, s/d = similar or different dihedral angles for the selected pair of aryls functionalized with -S(Me)-Au groups. [c] Dihedral angles after geometry optimization. Note the same input geometry was used in each case for both the calculations here using PBE and those in **Table S7** using B3LYP. [d] Where gap = LUMO – HOMO.

Table S7. Selected computational data for **Os1h**, **Si1h**, **C1h** models using the B3LYP functional.[a]

	s/d [b]	α (°) [c]	β (°) [c]	HOMO (eV)	LUMO (eV)	gap (eV) [d]	$4t^2$ (eV^2)
Os1h	s	56.7	56.2	−4.615	−1.675	2.940	-
	d	−64.8	0.5	−4.617	−1.692	2.925	-
Si1h	s	−38.8	−38.8	−5.641	−0.543	5.098	-
	d	−83.0	24.3	−5.629	−0.546	5.083	-
C1h	s	57.9	57.9	−5.404	−0.407	4.998	-
	d	−71.5	8.2	−5.542	−0.532	5.010	-
Os1h-Au_1	s	55.5	57.0	−4.064	−3.776	-	8.3×10^{-2}
	d	−55.5	−10.7	−4.090	−3.756	-	1.1×10^{-1}
Si1h-Au_1	s	−36.8	−37.0	−4.123	−3.895	-	5.2×10^{-2}
	d	−80.0	29.2	−4.166	−3.933	-	5.4×10^{-2}
C1h-Au_1	s	67.8	70.1	−4.174	−3.882	-	8.5×10^{-2}
	d	−74.7	13.0	−4.141	−3.909	-	5.4×10^{-2}

[a] Calculations performed as described in *Computational Details*. [b] Here, s/d = similar or different dihedral angles for the selected pair of aryls functionalized with -S(Me)-Au groups. [c] Dihedral angles after geometry optimization. Note the same input geometry was used in each case for both the calculations here using B3LYP and those in **Table S6** using PBE. [d] Where gap = LUMO – HOMO.

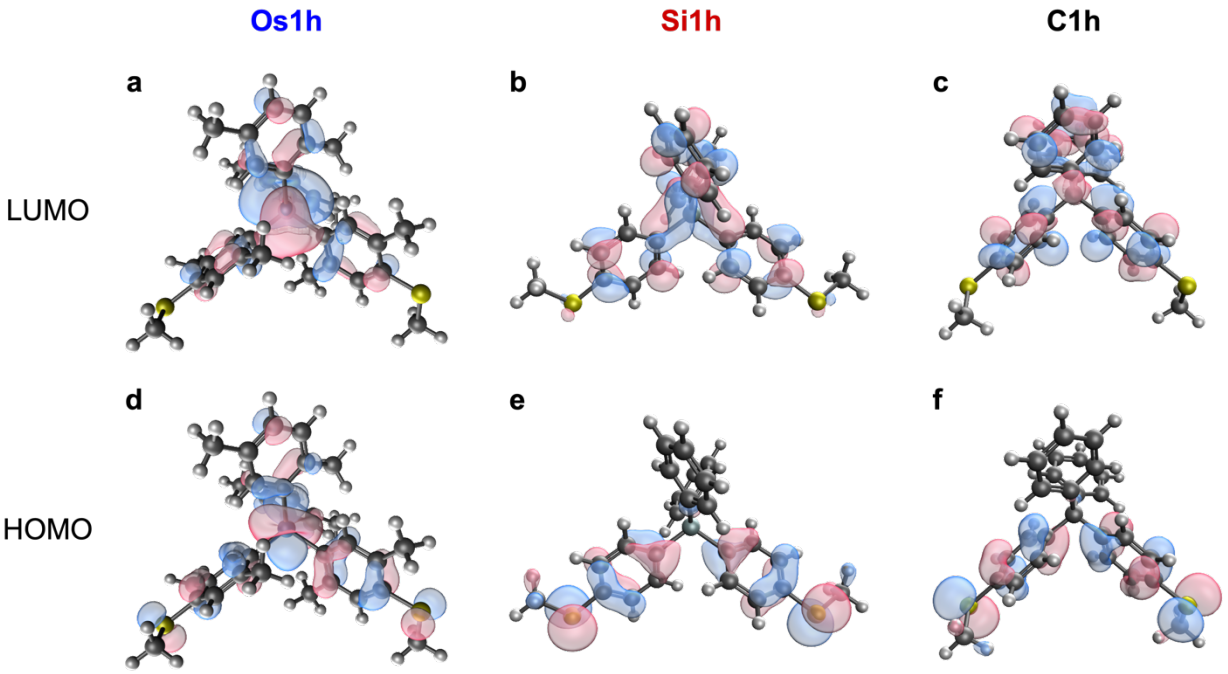

Figure S12. Isosurface plots of the **(a-c)** HOMO and **(d-e)** LUMO obtained from DFT calculations using B3LYP for gas phase **Os1**, **Si1**, and **C1** models (**Os1h**, **Si1h**, **C1h**, respectively; isovalue = 0.08 Å^{-3}). In each case, the HOMOs exhibit significant orbital density on the sulfur linkers, where the LUMOs do not, indicating these compounds should function as HOMO conductors. In **Os1h** there is a greater orbital density on the central atom (in this case, comprising an Os d_{z2} orbital rather than a C or Si sp^3 hybrid orbital). These plots corroborate the trends observed in the calculated transmission functions (**Figure S15**) and suggest the increased conductance of **Os1** relative to **Si1** or **C1** results from the extended delocalization of the thioanisole linker π-system across the central atom in the HOMO.

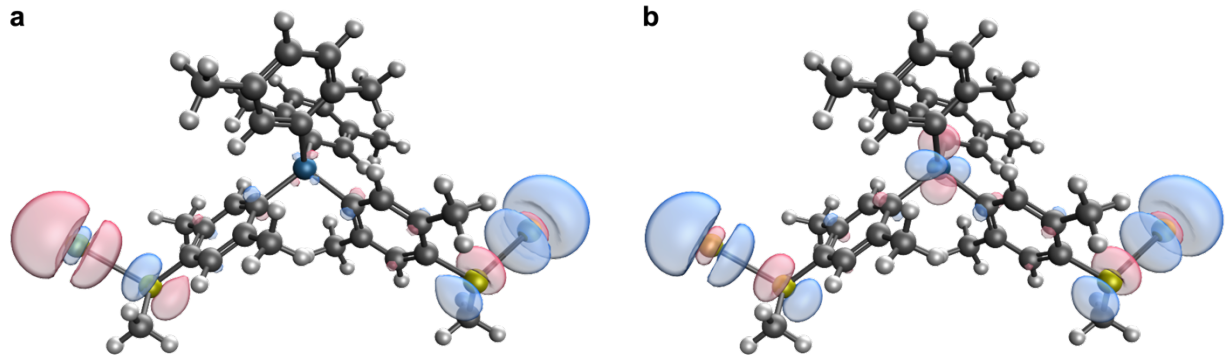

Figure S13. Isosurface plots of the **(a)** HOMO (antisymmetric) and **(b)** LUMO (symmetric) frontier orbitals obtained from DFT calculations using B3LYP for a **Os1** model (**Os1h**) bound to Au_1 clusters (isovalue = 0.08 Å^{-3}). These orbital plots are consistent with those observed in previous reports,[32,33] and illustrate how the Au s orbitals are tunnel coupled through the tetrahedral bridge.

Additional Quantum Transport Calculations Data (FHI-aims)

Table S8. HOMO-LUMO gaps (in eV) for the **Os-*n***, **Si-*n***, and **C-*n*** molecular series, calculated using the PBE and B3LYP functionals. We employed the same DFT computational parameters as described in *Section: General Information* of the **SI**. These computational parameters converge the HOMO-LUMO gaps within a window of 20 meV.

compound	PBE (eV)	B3LYP (eV)
Os1	1.560	2.862
Os2	1.660	2.963
Os3	1.723	3.077
Si1	3.400	4.808
Si2	2.948	4.269
Si3	2.740	4.021
C1	3.246	4.660
C2	2.985	4.301
C3	2.761	4.038

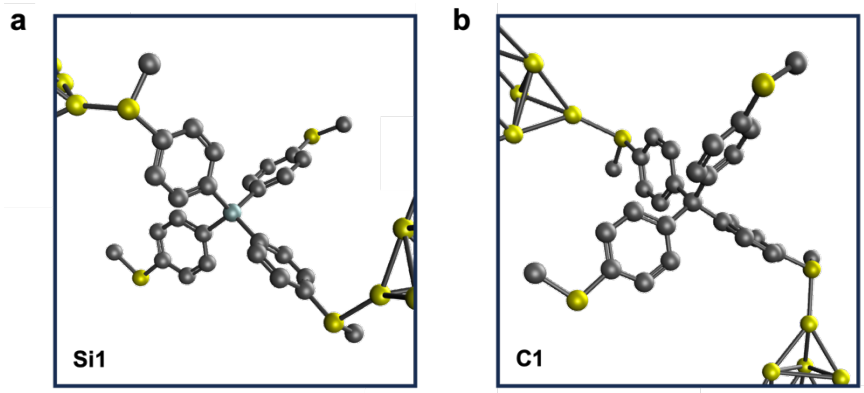

Figure S14. Additional representative junction geometries for **(b) Si1**, and **(c) C1**. Hydrogen atoms excluded for clarity.

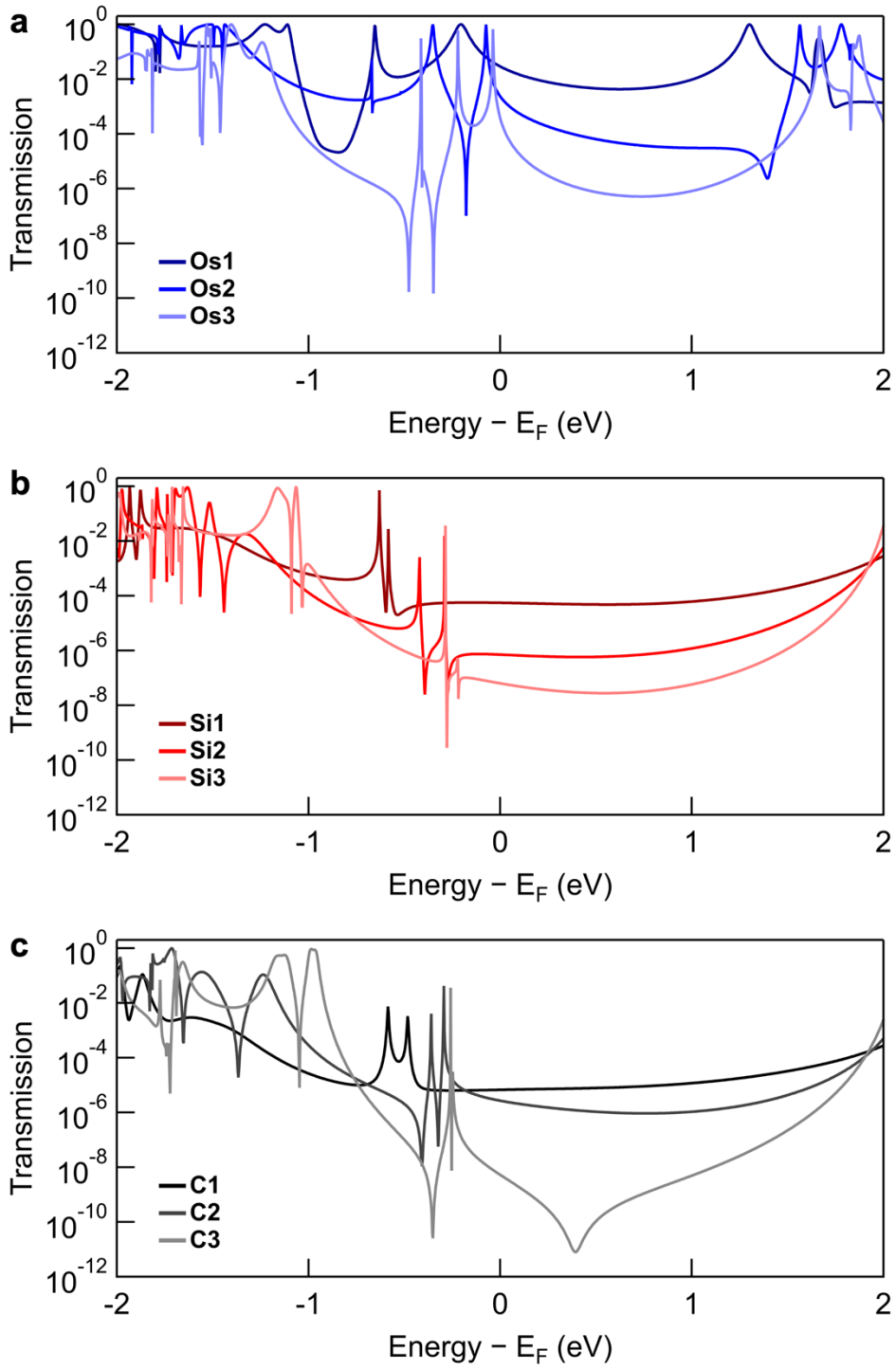

Figure S15. Overlaid calculated transmission functions for **(a) Os-*n***, **(b) Si-*n***, and **(c) C-*n***. Data for **Os-*n***, **Si2**, and **C2** are reproduced here from **Figure 5**, shown in an expanded format for clarity.

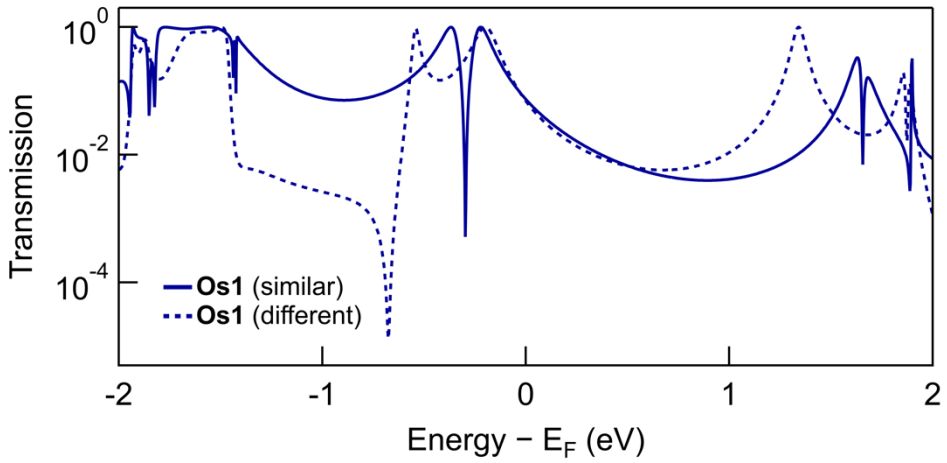

Figure S16. Transmission calculations for **Os1** junctions using the PBE functional, with electrodes connected at different -SMe contact groups. Here, the same geometries, having similar or different dihedral angles, were used as for the above tunnel coupling calculations. In contrast to those results above using Au_1 clusters with PBE, no significant changes in transmission at E_F are observed for these junctions with larger gold cluster electrodes.

7. NMR Spectra

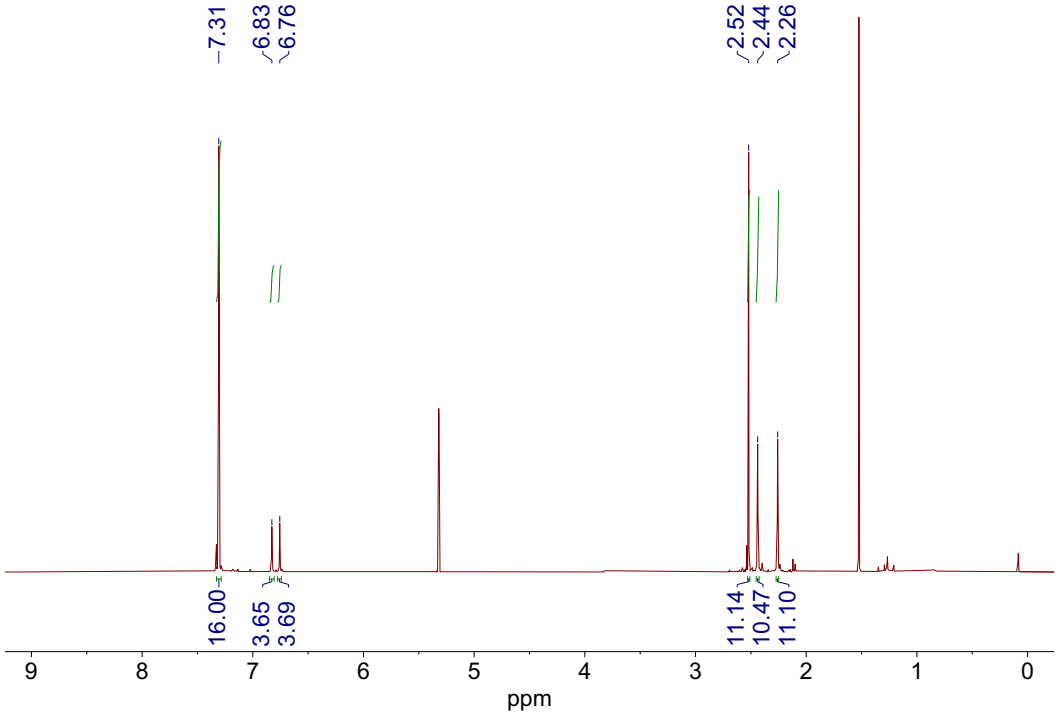

Figure S17. ^{1}H NMR (400 MHz) spectrum of **Os2** in CD_2Cl_2.

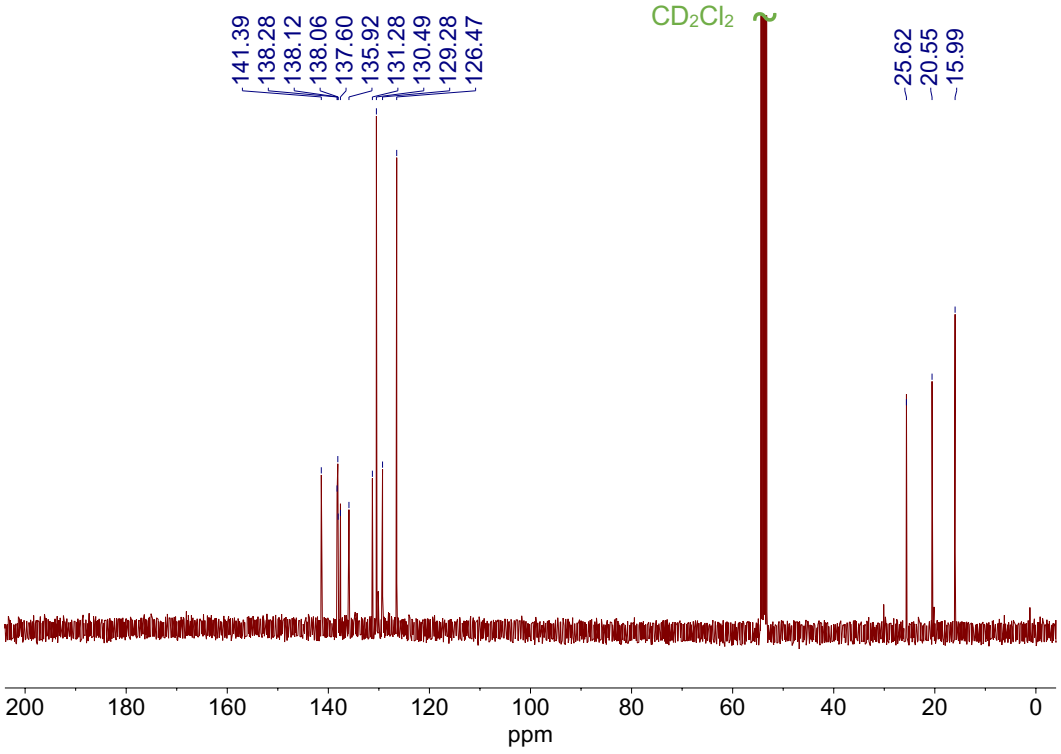

Figure S18. $^{13}C\{^{1}H\}$ NMR (100 MHz) spectrum of **Os2** in CD_2Cl_2.

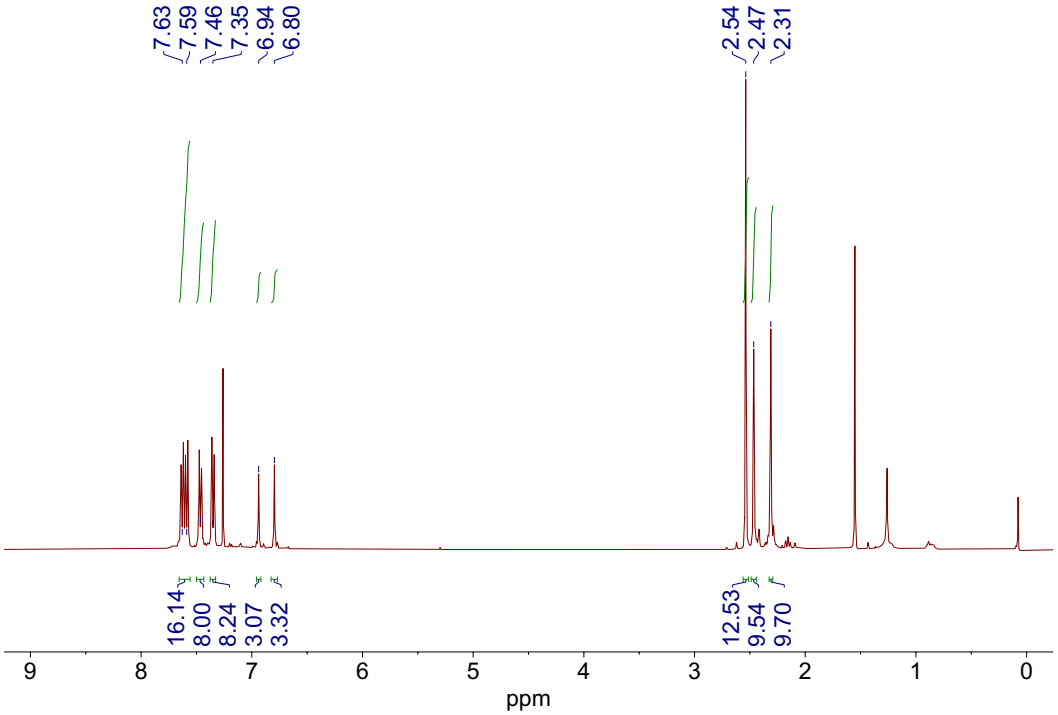

Figure S19. ^{1}H NMR (400 MHz) spectrum of **Os3** in $CDCl_3$.

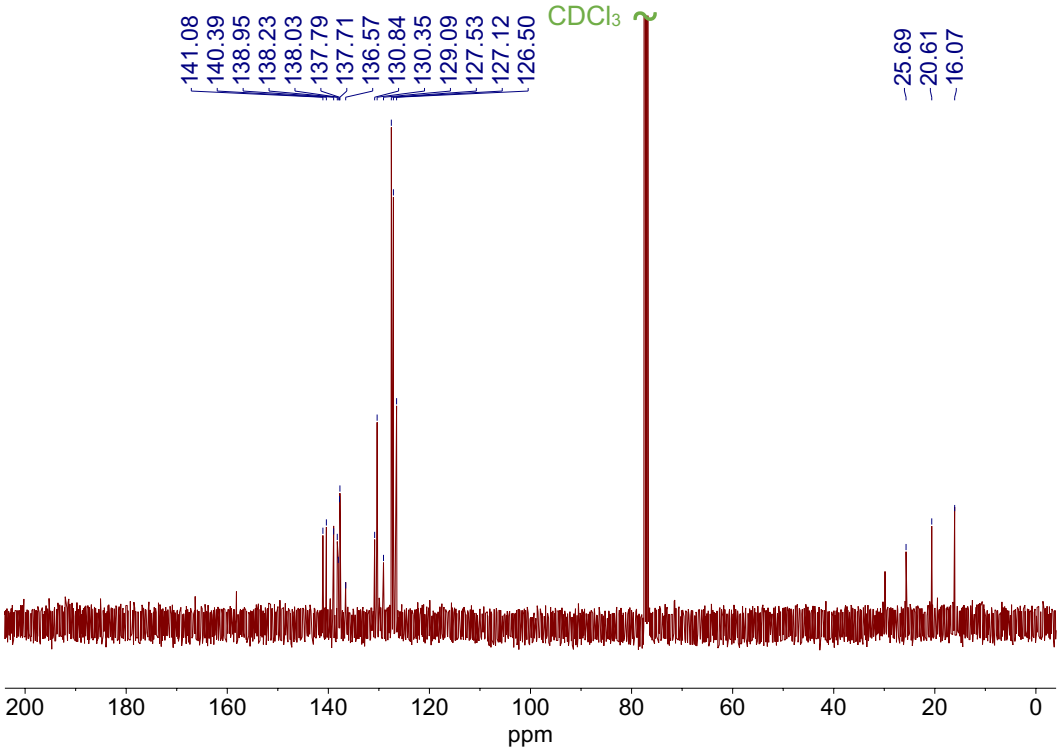

Figure S20. $^{13}C\{^{1}H\}$ NMR (101 MHz) spectrum of **Os3** in $CDCl_3$.

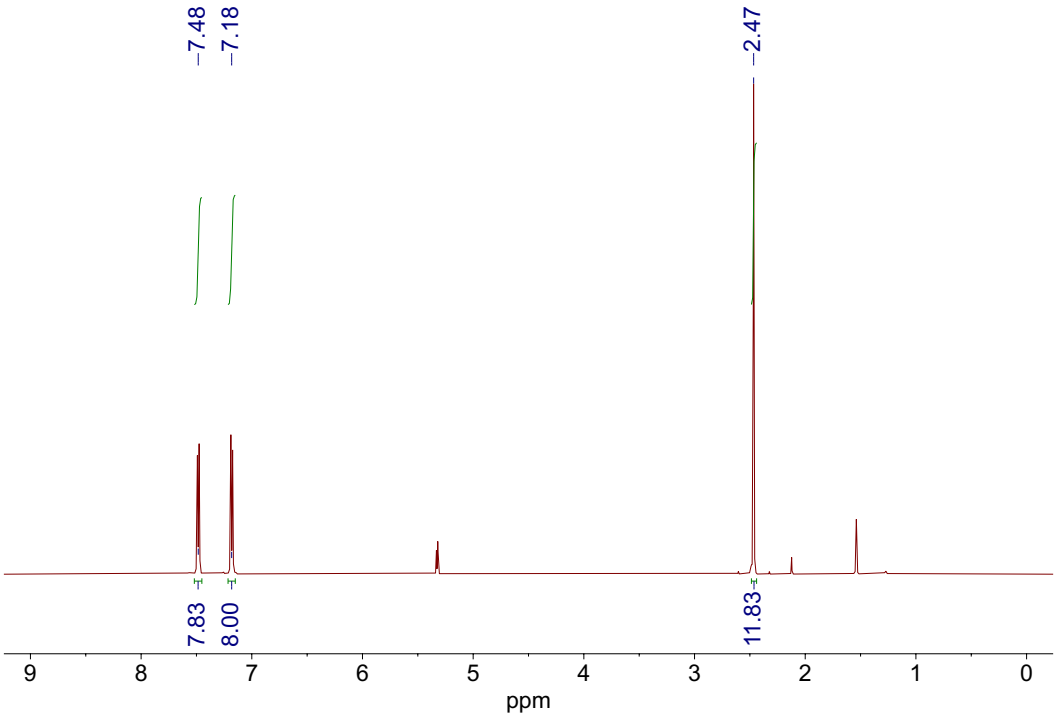

Figure S21. ^{1}H NMR (500 MHz) spectrum of **Si1** in CD_2Cl_2.

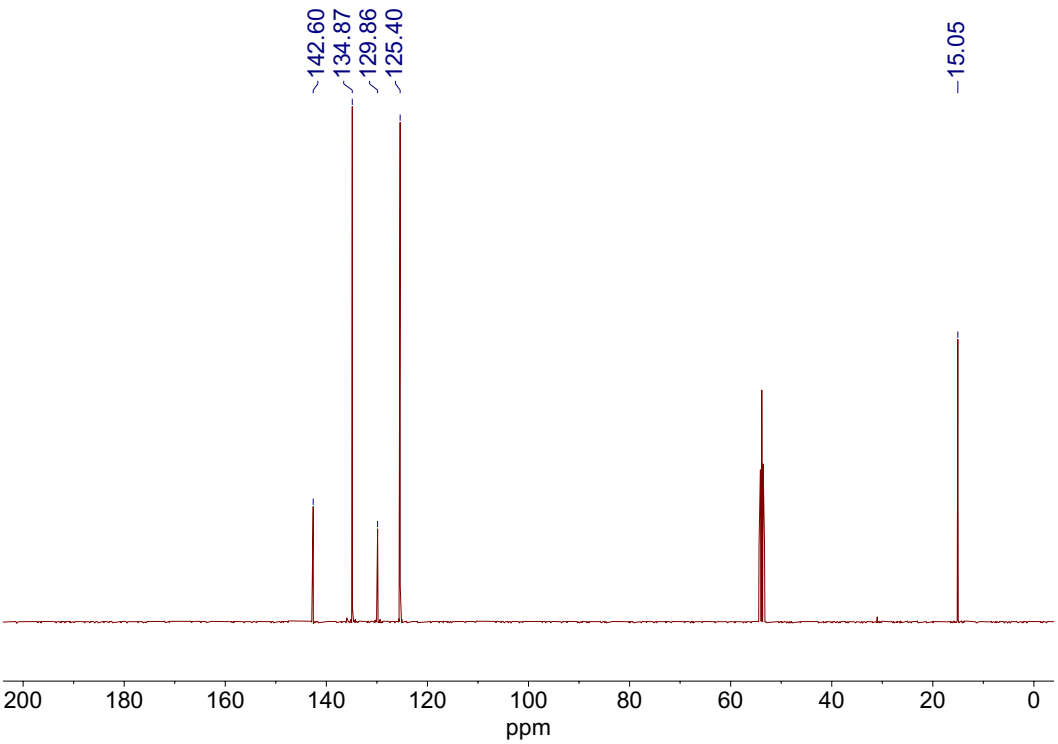

Figure S22. ^{13}C{^{1}H} NMR (101 MHz) spectrum of **Si1** in CD_2Cl_2.

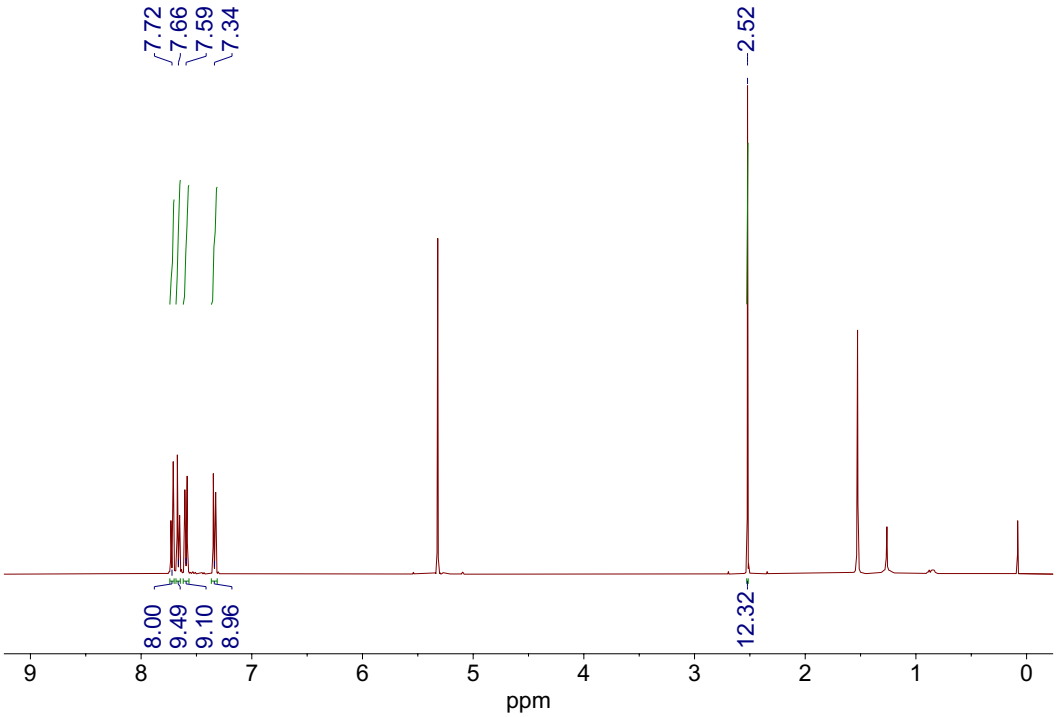

Figure S23. ^{1}H NMR (400 MHz) spectrum of **Si2** in CD_2Cl_2.

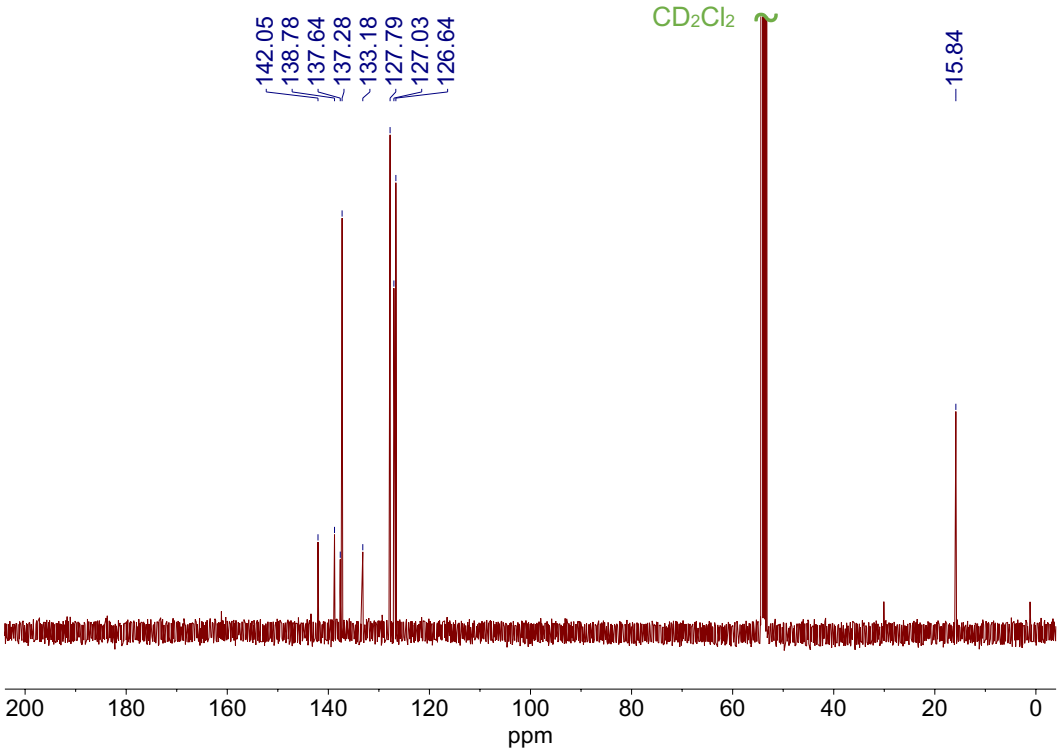

Figure S24. ^{13}C{^{1}H} NMR (101 MHz) spectrum of **Si2** in CD_2Cl_2.

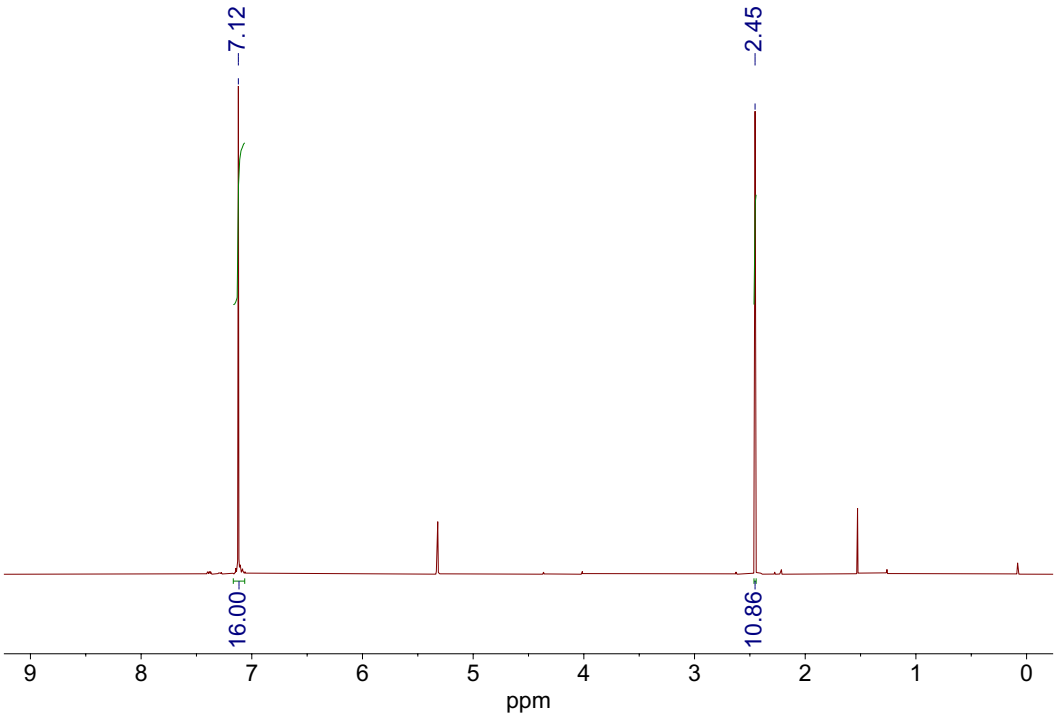

Figure S25. ^{1}H NMR (400 MHz) spectrum of **C1** in CD_2Cl_2.

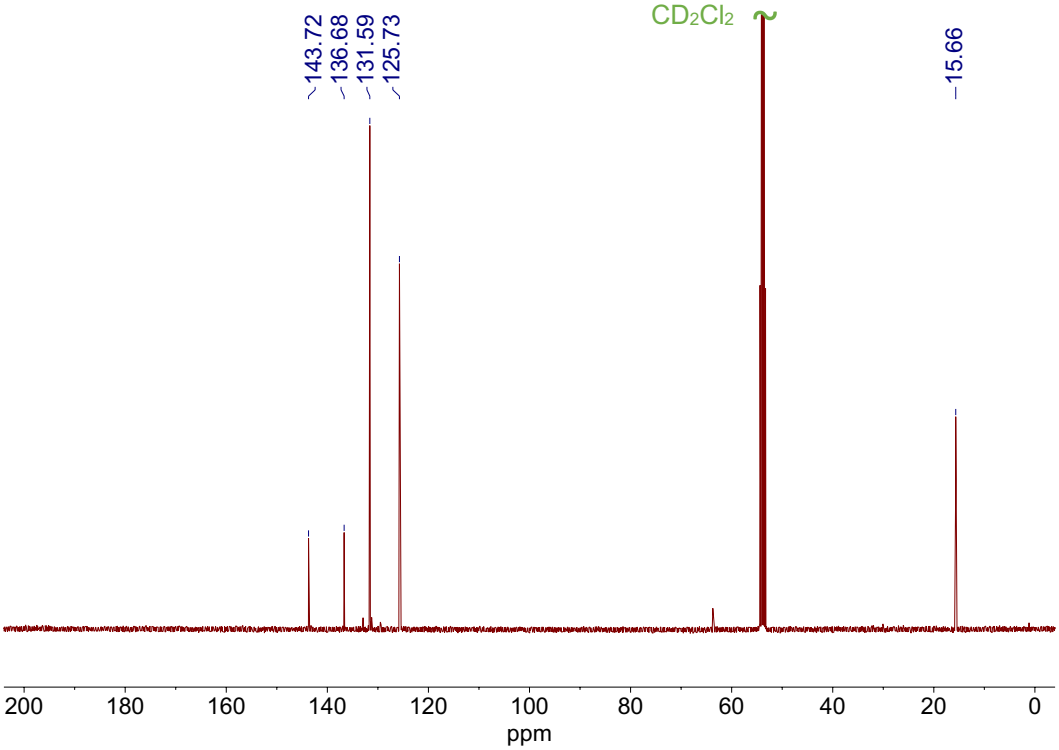

Figure S26. $^{13}C\{^{1}H\}$ NMR (150 MHz) spectrum of **C1** in CD_2Cl_2

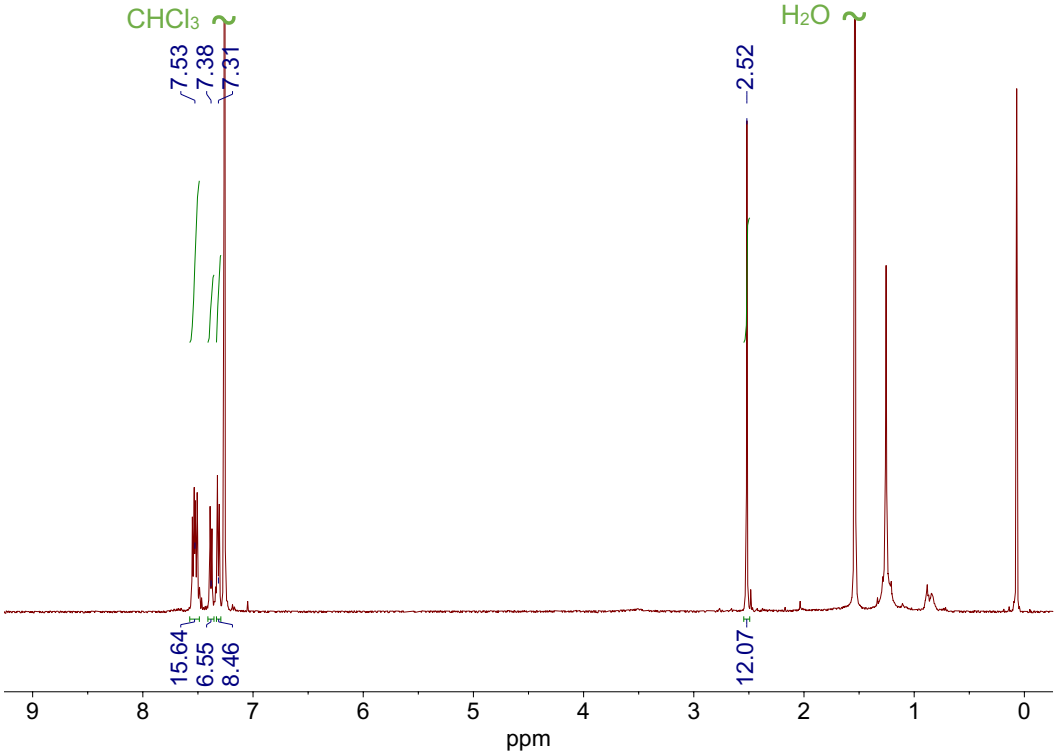

Figure S27. ^{1}H NMR (500 MHz) spectrum of **C2** in $CDCl_3$.

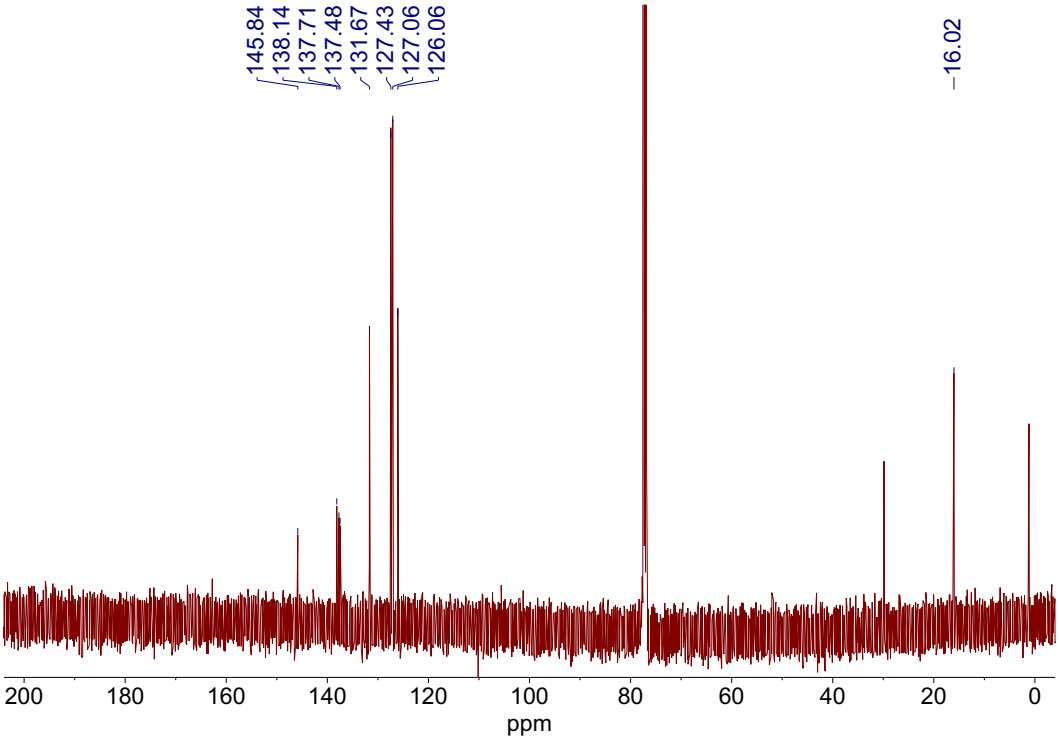

Figure S28. $^{13}C\{^{1}H\}$ NMR (126 MHz) spectrum of **C2** in $CDCl_3$.

7. References

(1) Williams, D. B. G.; Lawton, M. Drying of Organic Solvents: Quantitative Evaluation of the Efficiency of Several Desiccants. *J. Org. Chem.* **2010**, *75* (24), 8351–8354.

(2) Parr, J. M.; Olivar, C.; Saal, T.; Haiges, R.; Inkpen, M. S. Pushing Steric Limits in Osmium(IV) Tetraaryl Complexes. *Dalton Trans.* **2022**, *51* (27), 10558–10570.

(3) Love, B. E.; Jones, E. G. The Use of Salicylaldehyde Phenylhydrazone as an Indicator for the Titration of Organometallic Reagents. *J. Org. Chem.* **1999**, *64* (10), 3755–3756.

(4) Zagami, L.; Saal, T.; Avedian, C.; Inkpen, M. S. Intervalence Charge Transfer in an Osmium(IV) Tetra(Ferrocenylaryl) Complex. *Inorg. Chem.* **2025**, DOI: 10.1021/acs.inorgchem.4c04481.

(5) Yang, J.; He, W.; Denman, K.; Jiang, Y. B.; Qin, Y. A Molecular Breakwater-like Tetrapod for Organic Solar Cells. *J. Mater. Chem. A* **2015**, *3* (5), 2108–2119.

(6) Starr, R. L.; Fu, T.; Doud, E. A.; Stone, I.; Roy, X.; Venkataraman, L. Gold–Carbon Contacts from Oxidative Addition of Aryl Iodides. *J. Am. Chem. Soc.* **2020**, *142* (15), 7128–7133.

(7) Fulmer, G. R.; Miller, A. J. M.; Sherden, N. H.; Gottlieb, H. E.; Nudelman, A.; Stoltz, B. M.; Bercaw, J. E.; Goldberg, K. I. NMR Chemical Shifts of Trace Impurities: Common Laboratory Solvents, Organics, and Gases in Deuterated Solvents Relevant to the Organometallic Chemist. *Organometallics* **2010**, *29* (9), 2176–2179.

(8) Kim, L.; Czyszczon-Burton, T. M.; Nguyen, K. M.; Stukey, S.; Lazar, S.; Prana, J.; Miao, Z.; Park, S.; Chen, S. F.; Inkpen, M. S. Low Vapor Pressure Solvents for Single-Molecule Junction Measurements. *Nano Lett.* **2024**, *24* (32), 9998–10005.

(9) Venkataraman, L.; Klare, J. E.; Tam, I. W.; Nuckolls, C.; Hybertsen, M. S.; Steigerwald, M. L. Single-Molecule Circuits with Well-Defined Molecular Conductance. *Nano Lett.* **2006**, *6* (3), 458–462.

(10) Inkpen, M. S.; Liu, Z.; Li, H.; Campos, L. M.; Neaton, J. B.; Venkataraman, L. Non-Chemisorbed Gold–Sulfur Binding Prevails in Self-Assembled Monolayers. *Nature Chem.* **2019**, *11*, 351–358.

(11) Miao, Z.; Quainoo, T.; Czyszczon-Burton, T. M.; Rotthowe, N.; Parr, J. M.; Liu, Z.; Inkpen, M. S. Charge Transport across Dynamic Covalent Chemical Bridges. *Nano Lett.* **2022**, *22* (20), 8331–8338.

(12) Epifanovsky, E.; Gilbert, A. T. B.; Feng, X.; Lee, J.; Mao, Y.; Mardirossian, N.; Pokhilko, P.; White, A. F.; Coons, M. P.; Dempwolff, A. L.; Gan, Z.; Hait, D.; Horn, P. R.; Jacobson, L. D.; Kaliman, I.; Kussmann, J.; Lange, A. W.; Lao, K. U.; Levine, D. S.; Liu, J.; McKenzie, S. C.; Morrison, A. F.; Nanda, K. D.; Plasser, F.; Rehn, D. R.; Vidal, M. L.; You, Z. Q.; Zhu, Y.; Alam, B.; Albrecht, B. J.; Aldossary, A.; Alguire, E.; Andersen, J. H.; Athavale, V.; Barton, D.; Begam, K.; Behn, A.; Bellonzi, N.; Bernard, Y. A.; Berquist, E. J.; Burton, H. G. A.; Carreras, A.; Carter-Fenk, K.; Chakraborty, R.; Chien, A. D.; Closser, K. D.; Cofer-Shabica, V.; Dasgupta, S.; De Wergifosse, M.; Deng, J.; Diedenhofen, M.; Do, H.; Ehlert, S.; Fang, P. T.; Fatehi, S.; Feng, Q.; Friedhoff, T.; Gayvert, J.; Ge, Q.; Gidofalvi, G.; Goldey, M.; Gomes, J.; González-Espinoza, C. E.; Gulania, S.; Gunina, A. O.; Hanson-Heine, M. W. D.; Harbach, P. H. P.; Hauser, A.; Herbst, M. F.; Hernández Vera, M.; Hodecker, M.; Holden, Z. C.; Houck, S.; Huang, X.; Hui, K.; Huynh, B. C.; Ivanov, M.; Jász, Á.; Ji, H.; Jiang, H.; Kaduk, B.; Kähler, S.; Khistyaev, K.; Kim, J.; Kis, G.; Klunzinger, P.; Koczor-Benda, Z.; Koh, J. H.; Kosenkov,

D.; Koulias, L.; Kowalczyk, T.; Krauter, C. M.; Kue, K.; Kunitsa, A.; Kus, T.; Ladjánszki, I.; Landau, A.; Lawler, K. V.; Lefrancois, D.; Lehtola, S.; Li, R. R.; Li, Y. P.; Liang, J.; Liebenthal, M.; Lin, H. H.; Lin, Y. S.; Liu, F.; Liu, K. Y.; Loipersberger, M.; Luenser, A.; Manjanath, A.; Manohar, P.; Mansoor, E.; Manzer, S. F.; Mao, S. P.; Marenich, A. V.; Markovich, T.; Mason, S.; Maurer, S. A.; McLaughlin, P. F.; Menger, M. F. S. J.; Mewes, J. M.; Mewes, S. A.; Morgante, P.; Mullinax, J. W.; Oosterbaan, K. J.; Paran, G.; Paul, A. C.; Paul, S. K.; Pavošević, F.; Pei, Z.; Prager, S.; Proynov, E. I.; Rák, Á.; Ramos-Cordoba, E.; Rana, B.; Rask, A. E.; Rettig, A.; Richard, R. M.; Rob, F.; Rossomme, E.; Scheele, T.; Scheurer, M.; Schneider, M.; Sergueev, N.; Sharada, S. M.; Skomorowski, W.; Small, D. W.; Stein, C. J.; Su, Y. C.; Sundstrom, E. J.; Tao, Z.; Thirman, J.; Tornai, G. J.; Tsuchimochi, T.; Tubman, N. M.; Veccham, S. P.; Vydrov, O.; Wenzel, J.; Witte, J.; Yamada, A.; Yao, K.; Yeganeh, S.; Yost, S. R.; Zech, A.; Zhang, I. Y.; Zhang, X.; Zhang, Y.; Zuev, D.; Aspuru-Guzik, A.; Bell, A. T.; Besley, N. A.; Bravaya, K. B.; Brooks, B. R.; Casanova, D.; Chai, J. D.; Coriani, S.; Cramer, C. J.; Cserey, G.; Deprince, A. E.; Distasio, R. A.; Dreuw, A.; Dunietz, B. D.; Furlani, T. R.; Goddard, W. A.; Hammes-Schiffer, S.; Head-Gordon, T.; Hehre, W. J.; Hsu, C. P.; Jagau, T. C.; Jung, Y.; Klamt, A.; Kong, J.; Lambrecht, D. S.; Liang, W.; Mayhall, N. J.; McCurdy, C. W.; Neaton, J. B.; Ochsenfeld, C.; Parkhill, J. A.; Peverati, R.; Rassolov, V. A.; Shao, Y.; Slipchenko, L. V.; Stauch, T.; Steele, R. P.; Subotnik, J. E.; Thom, A. J. W.; Tkatchenko, A.; Truhlar, D. G.; Van Voorhis, T.; Wesolowski, T. A.; Whaley, K. B.; Woodcock, H. L.; Zimmerman, P. M.; Faraji, S.; Gill, P. M. W.; Head-Gordon, M.; Herbert, J. M.; Krylov, A. I. Software for the Frontiers of Quantum Chemistry: An Overview of Developments in the Q-Chem 5 Package. *J. Chem. Phys.* **2021**, *155*, 084801.

(13) Robbins, A.; Jeffrey, G. A.; Chesick, J. P.; Donohue, J.; Cotton, F. A.; Frenz, B. A.; Murillo, C. A. A Refinement of the Crystal Structure of Tetraphenylmethane: Three Independent Redeterminations. *Acta Crystallogr. B* **1975**, *31* (10), 2395–2399.

(14) Gruhnert, V.; Kirfel, A.; Will, G.; Wallrafen, F.; Recker, K. The Crystal Structure and Electron Density of Tetraphenyl-Silicon, $(C_6H_5)_4Si$. *Z. Krist.* **1983**, *163*, 53–60.

(15) Woitellier, S.; Launay, J. P.; Joachim. The Possibility of Molecular Switching: Theoretical Study of $[(NH_3)_5Ru\text{-}4,4'\text{-}Bipy\text{-}Ru(NH_3)_5]^{5+}$. *Chem Phys* **1989**, *131*, 481–488.

(16) Venkataraman, L.; Klare, J. E.; Nuckolls, C.; Hybertsen, M. S.; Steigerwald, M. L. Dependence of Single-Molecule Junction Conductance on Molecular Conformation. *Nature* **2006**, *442* (7105), 904–907.

(17) Blum, V.; Gehrke, R.; Hanke, F.; Havu, P.; Havu, V.; Ren, X.; Reuter, K.; Scheffler, M. Ab Initio Molecular Simulations with Numeric Atom-Centered Orbitals. *Comput. Phys. Commun.* **2009**, *180* (11), 2175–2196.

(18) Perdew, J. P.; Burke, K.; Ernzerhof, M. Generalized Gradient Approximation Made Simple. *Phys. Rev. Lett.* **1996**, *77* (18), 3865–3868.

(19) Lenthe, E. V.; Baerends, E. J.; Snijders, J. G. Relativistic Regular Two-Component Hamiltonians. *J. Chem. Phys.* **1993**, *99* (6), 4597–4610.

(20) Camarasa-Gómez, M.; Hernangómez-Pérez, D.; Evers, F. Spin–Orbit Torque in Single-Molecule Junctions from Ab Initio. *J. Phys. Chem. Lett.* **2024**, *15* (21), 5747–5753.

(21) Arnold, A.; Weigend, F.; Evers, F. Quantum Chemistry Calculations for Molecules Coupled to Reservoirs: Formalism, Implementation, and Application to Benzenedithiol. *J. Chem. Phys.* **2007**, *126* (17), 174101.

(22) Bagrets, A. Spin-Polarized Electron Transport Across Metal–Organic Molecules: A Density Functional Theory Approach. *J. Chem. Theory Comput.* **2013**, *9* (6), 2801–2815.
(23) Lau, M.-K.; Zhang, Q.-F.; Chim, J. L. C.; Wong, W.-T.; Leung, W.-H. Direct Functionalisation of σ-Aryl Ligands: Preparation of Homoleptic Functionalised Aryls of Osmium(Iv). *Chem. Commun.* **2001**, *79* (16), 1478–1479.
(24) Doud, E. A.; Inkpen, M. S.; Lovat, G.; Montes, E.; Paley, D. W.; Steigerwald, M. L.; Vázquez, H.; Venkataraman, L.; Roy, X. In Situ Formation of N-Heterocyclic Carbene-Bound Single-Molecule Junctions. *J. Am. Chem. Soc.* **2018**, *140* (28), 8944–8949.
(25) Olivar, C.; Parr, J. M.; Avedian, C.; Saal, T.; Zagami, L.; Haiges, R.; Sharma, M.; Inkpen, M. S. Osmium(IV) Tetraaryl Complexes Formed from Pre-Functionalized Ligands. *ChemRxiv* **2024**, DOI: 10.26434/chemrxiv-2024-2ksw1.
(26) Lau, M.-K. Transition Metal Complexes with Functionalized Aryl Ligands, Ph.D. Thesis, Hong Kong University of Science and Technology, 1999.
(27) Liu, X.-M.; He, C.; Xu, J.-W. Synthesis and Optical Properties of Tetraphenylmethane-Based Tetrahedral Fluorescent Compounds and Their Water-Soluble PEG-Linked Polymers. *Tetrahedron Lett.* **2004**, *45* (8), 1593–1597.
(28) Liu, X.-M.; He, C.; Huang, J.; Xu, J. Highly Efficient Blue-Light-Emitting Glass-Forming Molecules Based on Tetraarylmethane/Silane and Fluorene: Synthesis and Thermal, Optical, and Electrochemical Properties. *Chem. Mater.* **2005**, *17* (2), 434–441.
(29) Cheng, Z. L.; Skouta, R.; Vazquez, H.; Widawsky, J. R.; Schneebeli, S.; Chen, W.; Hybertsen, M. S.; Breslow, R.; Venkataraman, L. In Situ Formation of Highly Conducting Covalent Au-C Contacts for Single-Molecule Junctions. *Nature Nanotechnol.* **2011**, *6* (6), 353–357.
(30) Li, Y.; Zhao, C.; Wang, R.; Tang, A.; Hong, W.; Qu, D.; Tian, H.; Li, H. In Situ Monitoring of Transmetallation in Electric Potential-Promoted Oxidative Coupling in a Single-Molecule Junction. *CCS Chem.* **2022**, *5*, 191–199.
(31) Fatemi, V.; Kamenetska, M.; Neaton, J. B.; Venkataraman, L. Environmental Control of Single-Molecule Junction Transport. *Nano Lett.* **2011**, *11* (5), 1988–1992.
(32) Venkataraman, L.; Park, Y. S.; Whalley, A. C.; Nuckolls, C.; Hybertsen, M. S.; Steigerwald, M. L. Electronics and Chemistry: Varying Single-Molecule Junction Conductance Using Chemical Substituents. *Nano Lett.* **2007**, *7* (2), 502–506.
(33) Prana, J.; Kim, L.; Czyszczon-Burton, T.; Homann, G.; Chen, S.; Miao, Z.; Camarasa-Gomez, M.; Inkpen, M. Lewis-Acid Mediated Reactivity in Single-Molecule Junctions. *J. Am. Chem. Soc.* **2024**, *146* (48), 33265–33275.